



Measurement, Characterization, and Modeling of Initial Geometric Imperfections in Wide-Flange Steel Members Subjected to Combined Axial and Cyclic Lateral Loading

Omar A. Sediek, S.M.ASCE¹; Tung-Yu Wu, Ph.D., M.ASCE²; Ting-Hao Chang³; Jason McCormick, Ph.D., P.E., M.ASCE⁴; and Sherif El-Tawil, Ph.D., P.E., F.ASCE⁵

Abstract: Wide-flange (W-shape) steel members are known to have initial geometric imperfections. A three-dimensional noncontact laser-scanning technique is used to measure the imperfection fields in fourteen specimens. A spectral approach that models the imperfections in each plate of the W-shape member as a two-dimensional random field is employed to characterize the imperfections and capture the existence of periodicity in them. The proposed modeling approach along with the traditional modal approach are used to study the sensitivity of numerical models to initial geometric imperfections. The studies are conducted at both member and system levels using a set of column and frame models employing deep W-shape columns under combined axial and lateral cyclic loading. It is shown that although initial geometric imperfections can, in certain situations, influence column buckling behavior as well as frame collapse mode, their effect on nonlinear cyclic behavior is generally small and inconsistent. Based on this finding, it is recommended that initial geometric imperfections need not be incorporated in high-fidelity numerical models of W-shape members subjected to combined axial and cyclic lateral loads. However, this is conditioned upon the use of a computational platform with sufficient numerical precision to capture the early small deformations that promote geometric nonlinearity in the response. **DOI:** 10.1061/(ASCE)ST.1943-541X.0003086. © 2021 American Society of Civil Engineers.

Introduction

Initial geometric imperfections (IGIs) are introduced into wideflange (W-shape) steel structural members during manufacturing, shipping, and construction. It is common practice in finite element modeling to account for IGIs by superimposing a preassumed displacement field onto the mesh geometry. The amplitude of the superimposed field, which is the maximum deviation of the real member from the nominal shape of the member, is generally selected based on manufacturing tolerances, e.g., in AISC 303 (AISC 2016a) and ASTM A6 (ASTM 2019).

IGIs in W-shape members can be categorized into global and local imperfections. Current finite element modeling practice for earthquake engineering typically accounts for both categories. Global IGIs are generally assumed to follow a half sine wave with a maximum amplitude that ranges from L/1,500 to L/500 at member midheight, where L is the length of the member. These

Note. This manuscript was submitted on June 16, 2020; approved on April 2, 2021; published online on June 18, 2021. Discussion period open until November 18, 2021; separate discussions must be submitted for individual papers. This paper is part of the *Journal of Structural Engineering*, © ASCE, ISSN 0733-9445.

numbers bracket the allowable limit of L/960 for hot-rolled steel columns specified in ASTM A6 (ASTM 2019). The distribution of local IGIs is generally assumed to be a combination of the first few local buckling modes with a maximum amplitude of $b_f/250$ or h/250, where b_f and h are the flange width and web depth of the member, respectively. As with global IGIs, these numbers originate from manufacturing tolerances in current specifications, e.g., AISC 303 (AISC 2016a). Examples of the various practices for modeling IGIs in W-shapes can be found in Fogarty and El-Tawil (2015), Elkady and Lignos (2015), Fogarty et al. (2017), Elkady and Lignos (2018), Wu et al. (2018a), Sediek et al. (2020b), and Cravero et al.

The current way of incorporating IGIs in W-shape members using assumed deterministic imperfection fields is a convenient one to implement. However, it is not clear how closely the assumed IGI fields match the actual imperfections in real members, and if not, how important it is to accurately model the real IGI fields in finite elements analysis of structures under seismic loading. Previous studies that measured IGI fields in steel components focused on cold-formed members (e.g., Schafer and Peko 1998; Cruise and Gardner 2006; McAnallen et al. 2014; Zhao et al. 2015; Selvaraj and Madhavan 2018). To the authors' knowledge, IGI fields have not yet been measured and characterized for W-shape steel members. Also, no studies have comprehensively investigated the effects of incorporating different IGI approaches on the computational response of W-shape steel columns subjected to combined axial and lateral loads, as occurs under earthquake loading.

To address the identified research gaps, a three-dimensional (3D) noncontact laser-scanning technique is employed to measure the initial global and local geometric imperfections in fourteen Taiwanese hot-rolled H-section steel members that have similar cross-sectional properties to deep W-shape members used in the US. The measured imperfections are then used to characterize initial IGIs in W-shape steel members using a spectral approach that characterizes IGIs as a random field superimposed on the ideal geometry of the

¹Ph.D. Candidate, Dept. of Civil and Environmental Engineering, Univ. of Michigan, Ann Arbor, MI 48109-2125. ORCID: https://orcid.org/0000-0002-3369-2598. Email: osediek@umich.edu

²Assistant Professor, Dept. of Civil Engineering, National Taiwan Univ., Taipei 10617, Taiwan (corresponding author). ORCID: https://orcid.org/0000-0002-2981-1910. Email: tungyuwu@ntu.edu.tw

³Graduate Student, Dept. of Civil Engineering, National Taiwan Univ., Taipei 10617, Taiwan. Email: r08521235@ntu.edu.tw

⁴Associate Professor, Dept. of Civil and Environmental Engineering, Univ. of Michigan, Ann Arbor, MI 48109-2125. ORCID: https://orcid.org/0000-0002-7379-4660. Email: jpmccorm@umich.edu

⁵Professor, Dept. of Civil and Environmental Engineering, Univ. of Michigan, Ann Arbor, MI 48109-2125. ORCID: https://orcid.org/0000-0001-6437-5176. Email: eltawil@umich.edu

specimen. Modeling recommendations for incorporating IGIs in numerical simulations are proposed, then used to integrate IGIs into two types of numerical models: member level (i.e., single column) and system level (i.e., special moment frame). The computational results are used to study the effect of incorporating IGIs in simulation models using the traditional modal approach from the literature and the proposed modeling approach, which is based on measured data.

Imperfection Measurement

Specimens Selection

Deep W-shape columns (W24 or deeper) are widely used in special moment frames (SMFs) in the US to provide highly ductile behavior, as specified in the AISC Seismic Provisions (AISC 2016b), during an earthquake. Seven Taiwanese hot-rolled H-sections with dimensions similar to deep W-shape sections often used as columns in the US are considered in duplicate, for a total of fourteen members. The sections are selected to cover a wide range of parameters, including local and global slenderness ratios. The chosen sections are shown in Fig. 1 (circled squares) along with comparable deep W-shape sections used in the US (black diamonds). The measured specimens are made of SN490B steel ($F_v = 325$ MPa) and have a length of 1,800 mm with the cross-sectional properties listed in Table 1. The specimens are designated as $d \times b_f$ - duplicate number. For example, Specimen $150 \times 75 - 1$ is the first duplicate of the $150 \times 75 \times 5 \times 7$ section (d = 150 mm, $b_f = 75$ mm, $t_w = 5$ mm, and $t_f = 7$ mm).

The measured specimens can be classified into three types based on their local slenderness ratios: $b_f/2t_f$ and h/t_w (b_f and t_f are the flange width and thickness, respectively, and h and t_w are the web depth and thickness, respectively) and the AISC high ductility limits (HDLs) for W-shape columns (AISC 2016b), as shown in Fig. 1. Type I specimens satisfy the HDLs for both $b_f/2t_f$ and h/t_w and can exhibit highly ductile behavior for any axial load level up to

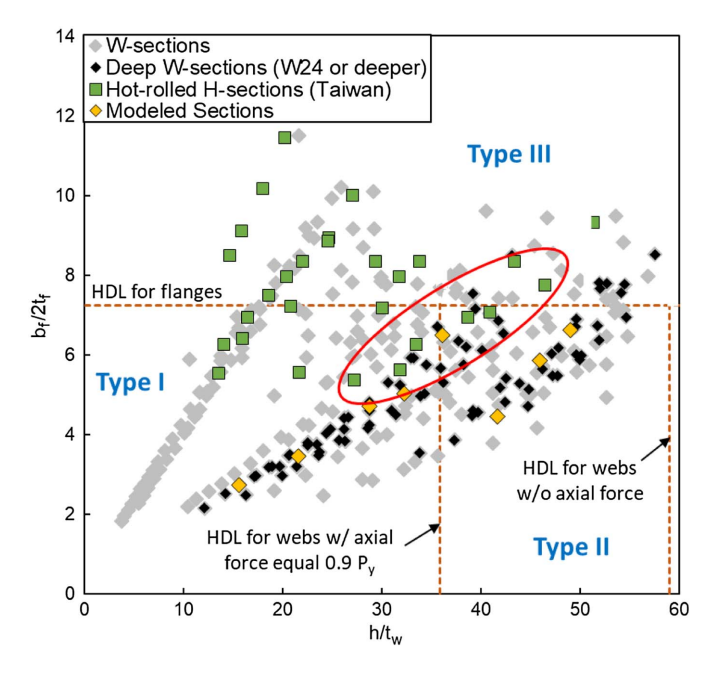


Fig. 1. Local slenderness ratios of sections used in the measurements (circled squares).

Table 1. Properties of measured hot rolled H-sections (all dimensions in mm)

Hot rolled H-section	d	b_f	t_w	t_f	r_{y}	$b_f/2t_f$	h/t_w	L/r_y
$150 \times 75 \times 5 \times 7$	150	75	5.0	7.0	1.66	5.4	27	108
$175 \times 90 \times 5 \times 8$	175	90	5.0	8.0	2.06	5.6	32	87
$198 \times 99 \times 5 \times 8$	198	99	5.0	8.0	2.24	6.2	36	80
$200\times100\times5.5\times8$	200	100	5.5	8.0	2.24	6.3	33	80
$248 \times 124 \times 5 \times 8$	248	124	5.0	8.0	282	7.8	46	64
$250 \times 125 \times 6 \times 9$	250	125	6.0	9.0	2.82	6.9	39	64
$300\times150\times6.5\times9$	300	150	6.5	9.0	3.29	8.3	43	55

 $0.9P_y$, where P_y is the axial yield capacity. Type II specimens are highly ductile only for specific axial load ratios based on h/t_w . Type III specimens are not highly ductile based on their $b_f/2t_f$ ratios. For more information about the characteristics of the different types of W-shape sections, the reader is referred to Fogarty and El-Tawil (2015). The global slenderness ratio around the weak axis of the measured specimens (L/r_y) ranges from 55 to 108.

Measurement Technique

The specimens are first carefully cleaned of dirt and rust and then painted. A 3D noncontact laser-scanning technique, which has been widely used in different fields (Almutairi et al. 2018; Lee et al. 2020), is used to capture the IGIs. This technique is able to capture the complete geometric profile of the measured specimen with an accuracy of 0.048 mm. Each specimen is placed horizontally on a concrete block as shown in Fig. 2(a). The 3D laser scanner (Faro Quantum M Scan Arm, Faro, Lake Mary, Florida) is used to scan each specimen, providing a 3D point cloud for it. The scanning arm has two folds, as shown in Fig. 2(a). This configuration allows for scanning of specimens with lengths up to 2.5 m by placing the scanning arm on a tripod at the midspan of the specimen. The arm can then be moved on either side of the measured specimen. The articulated scanning arm is a seven-axis arm [three joint translations combined with four joint rotations (360°)] with a spherical working volume to allow full three-dimensional movement of the attached scanning probe at the end of the arm. It has rotary optical encoders on each of its joints. The point cloud is sent to the host computer by processing the signals from these encoders using an error coding and temperature compensation technology (FARO 2016). The measurements were processed at a scan rate of 600,000 points/s and took an hour for each specimen on average.

The scanning work is performed manually by guiding the scanning arm along the length of the measured specimen. Only the outer surface of the specimens is measured, which is sufficient for the purposes of this study. Figs. 2(b and c) show 3D and cross-sectional measurements for Specimen $248 \times 124 - 1$, respectively. The employed measurement technique provides detailed information about the complete geometric profile of the measured specimens that is then used to characterize the IGIs.

Data Processing

The process of extracting the IGI profiles from the specimen measurements starts with creating 3D models of the ideal specimens using the computer-aided drawing (CAD) software Auto-CAD version 2018 (AutoDesk 2018). The measured data, which are uniformly distributed by specifying a minimum distance between points, is superimposed on the ideal 3D models of the specimens using the iterative least-square method (best-fit alignment) integrated in PolyWorks version 2020 software. The deviation of measured data from the ideal model, i.e., the IGI profile, is

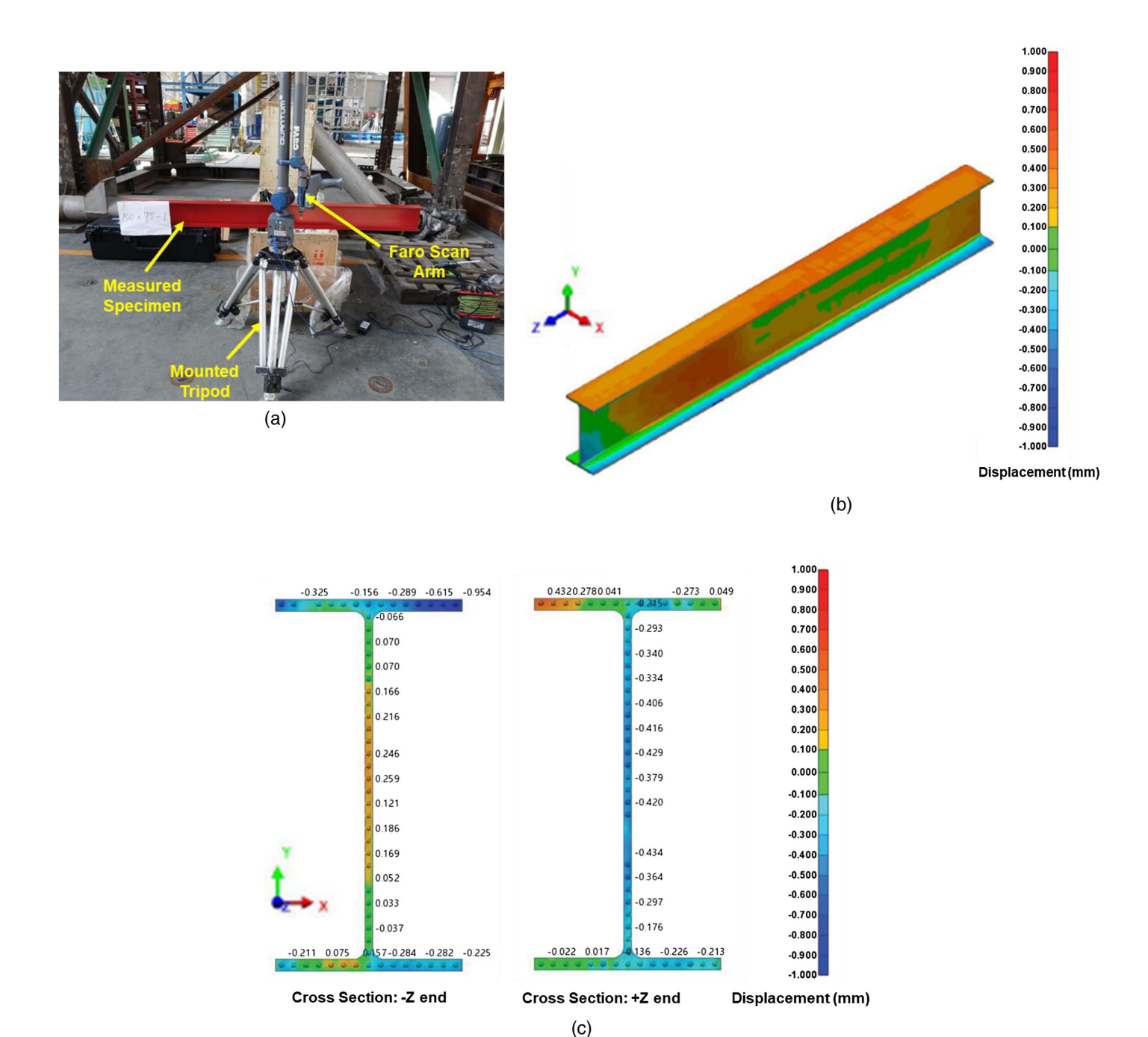


Fig. 2. Illustration of (a) measurement setup; (b) 3D measurements of Specimen $248 \times 124 - 1$; and (c) cross-sectional measurements of Specimen $248 \times 124 - 1$ (all units are millimeters).

extracted with respect to a designated coordinate system, as seen in Figs. 2(b and c). The coordinates of the measured cross-sectional points on the specimens are extracted every 10 mm through the length of the specimens, resulting in 179 cross sections for each specimen. Fig. 3(a) shows the point cloud of an arbitrary cross section of Specimen $175 \times 90 - 1$. It should be noted that there are a few cross sections that have only a few or even no points at one corner of one of the flanges. To avoid this issue, these problematic cross sections are detected and replaced using shape-preserving piecewise cubic spline interpolation through the length of the specimen.

The midline of each cross section is obtained as shown in Fig. 3(a) in order to assess the amount of imperfection along the length of the members (to exclude the effect of thickness

variation) and create finite element models using shell elements. The midline of each cross section contains a total of 21 points, distributed as seven points in each of the two flanges and seven points in the web, with two additional common points between the web and the flanges [Points 4 and 11 in Fig. 3(b)]. The two-dimensional (2D) coordinates of the 21 points on the midline of each cross section extracted from measured data are compared to the ones extracted from the 3D ideal models as shown in Fig. 3(b). The IGI is defined as the difference (in *x*- and *y*-directions) between the coordinates of the measured and ideal points.

The measured geometric imperfections (termed δ_1 – δ_{21}) are separated into three groups depending on the member element: top flange (δ_1 – δ_7), bottom flange (δ_8 – δ_{14}), and web (δ_{15} – δ_{21}), with

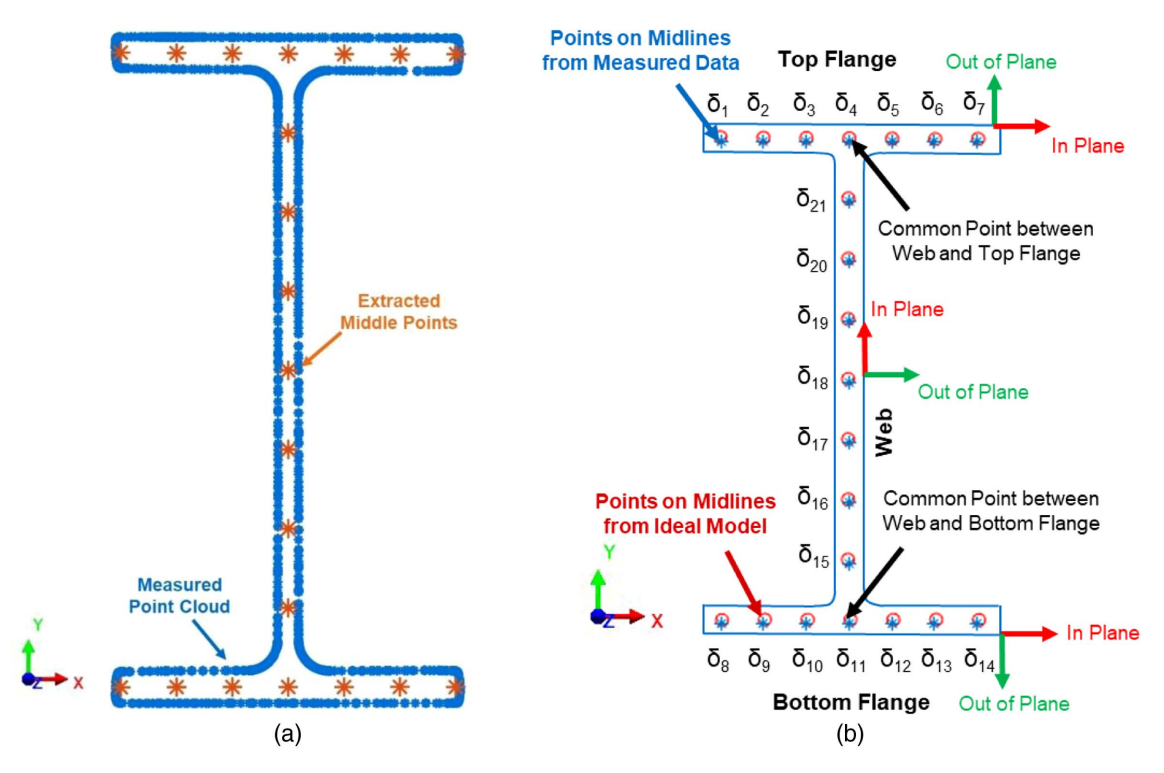


Fig. 3. Illustration of (a) measured point cloud for an arbitrary cross section of Specimen $175 \times 90 - 1$; and (b) initial imperfection measurement for an arbitrary cross section of Specimen $150 \times 75 - 1$.

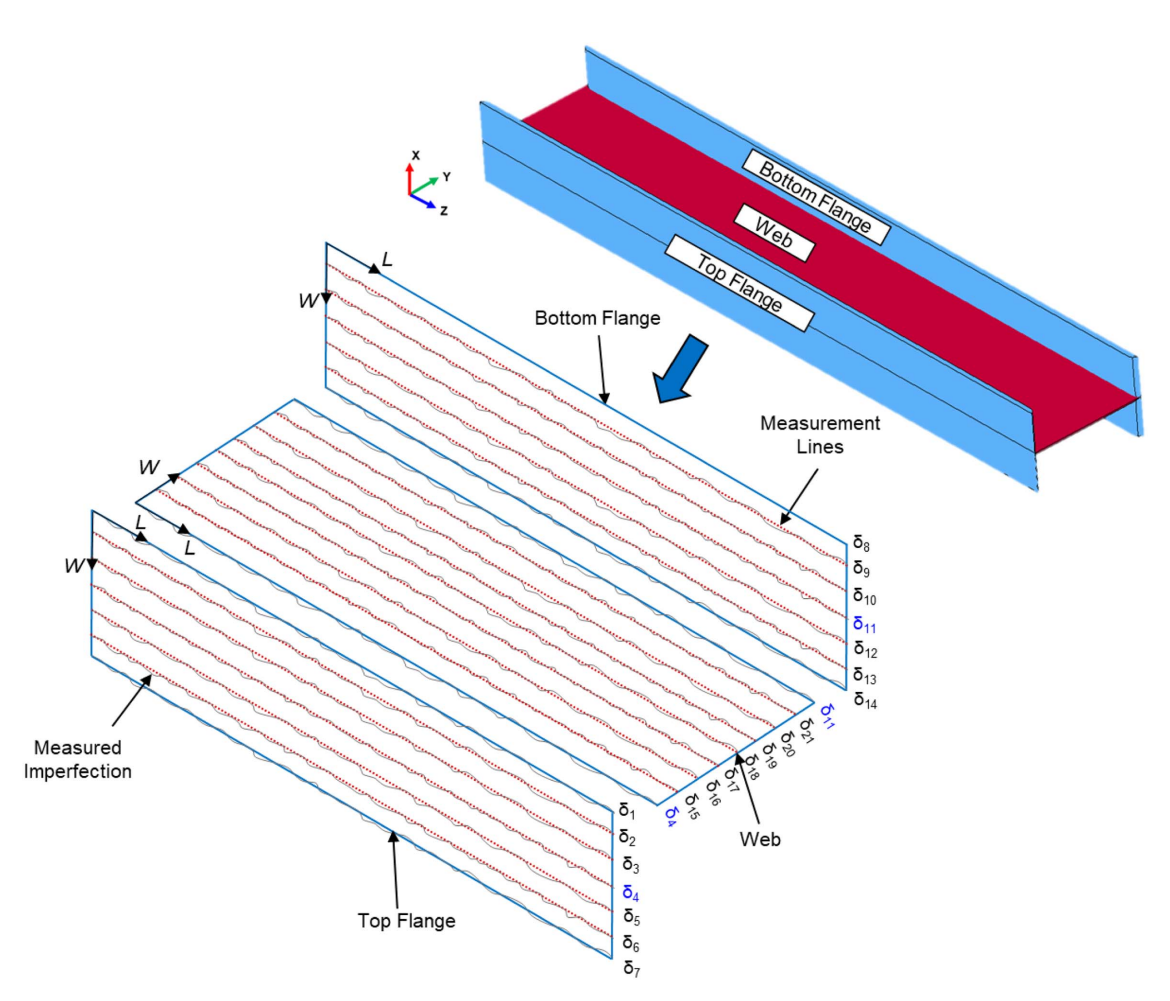


Fig. 4. Imperfection measurement locations along top flange, bottom flange, and web plates.

 δ_4 and δ_{11} as the two common points between the web and flanges as shown in Fig. 3(b). Each imperfection group is separated into two categories: in-plane and out-of-plane. For the flanges, the differences between the coordinates of the measured and ideal points in the x- and y-direction, e.g., δ_{7x} and δ_{7y} at δ_{7} , are defined as the inplane and out-of-plane imperfection, respectively [Fig. 3(b)]. For the web, the directions of the in-plane and out-of-plane imperfections are opposite to those described for the flanges as shown in Fig. 3(b). The previously described procedures are repeated for each cross section through the length of the measured specimens as shown in Fig. 4, resulting in an imperfection profile, which is a deviation plot for each point over the length of the member. In total, there are 21×2 imperfection profiles for each specimen (including both in-plane and out-of-plane profiles). It should be noted that the deflection resulting from the member's self-weight is subtracted from the profiles, although it was extremely small compared with the measured imperfections (i.e., with maximum of 0.0022 mm). The specimens are assumed to be cantilevered from both sides of the concrete block when evaluating the deflection resulting from the member's self-weight. Fig. 5 shows the out-of-plane imperfection profiles for the top flange of Specimen $150 \times 75 - 1$. As shown, few high-frequency noise signals exist in the measurements. However, these high-frequency noise signals are not the dominant frequencies in the measured imperfection signals, as will be discussed later. It is clear from Fig. 5 that the measured imperfection profiles do not compare well to the global and local buckling modes traditionally used to model IGIs in W-shape steel members.

Comparison with Specification Limits

The maximum measured imperfections are compared to the permitted variations in W-shape members indicated in the Standard Specification for General Requirements for Rolled Structural Steel Bars, Plates, Shapes, and Sheet Piling [ASTM A6 (ASTM 2019)] as well as the Dimensions, Mass, and Permissible Variations of Hot Rolled Steel Sections in Taiwan (CNS 2012). The permitted geometric variations for W-shape members (i.e., IGIs) are classified into local cross-sectional and global variations. The local cross-sectional variations are defined through the variation in section depth (Δd), variation in flange width (Δb_f) , flange out-of-square (T+T'), web out-of-center (E), and maximum depth at any cross section over theoretical depth (c). The definition of each variation is illustrated graphically in Fig. 6(a). The global variations are defined through either the maximum global variation around the strong axis (i.e., camber) or around the weak axis (i.e., sweep) as shown in Figs. 6(b and c), respectively.

The mean, maximum, and standard deviation of the measured Δd , Δb_f , T+T', E, C, sweep, and camber are evaluated among the fourteen specimens using Eqs. (1)–(7) and listed in Table 2 with the corresponding allowable values as specified in both ASTM (2019) and CNS (2012). As shown, all of the measured imperfections fall within the allowable specified limits. In fact, the mean measured imperfections are far from the allowable limits in ASTM (2019) and CNS (2012), which implies that using the allowable tolerances as maximum amplitude for IGIs in numerical models of W-shape members is not always realistic

$$\Delta d = \delta_{4y} - \delta_{11y} \tag{1}$$

$$\Delta b_f = \begin{cases} \sqrt{(b_f + \delta_{7x} - \delta_{1x})^2 + (\delta_{7y} - \delta_{1y})^2} - b_f, & \text{top flange} \\ \sqrt{(b_f + \delta_{14x} - \delta_{8x})^2 + (\delta_{14y} - \delta_{8y})^2} - b_f & \text{bottom flange} \end{cases}$$
(2)

$$T + T' = |\delta_{7y} - \delta_{1y}| + |\delta_{14y} - \delta_{8y}| \tag{3}$$

$$E = \begin{cases} \max \begin{cases} \sqrt{\left(\frac{b_{f}}{2} + \delta_{7x} - \delta_{4x}\right)^{2} + (\delta_{7y} - \delta_{4y})^{2}} - \frac{b_{f}}{2} \\ \sqrt{\left(\frac{b_{f}}{2} + \delta_{4x} - \delta_{1x}\right)^{2} + (\delta_{4y} - \delta_{1y})^{2}} - \frac{b_{f}}{2} \end{cases}, & \text{top flange} \\ \max \begin{cases} \sqrt{\left(\frac{b_{f}}{2} + \delta_{14x} - \delta_{11x}\right)^{2} + (\delta_{14y} - \delta_{11y})^{2}} - \frac{b_{f}}{2} \\ \sqrt{\left(\frac{b_{f}}{2} + \delta_{11x} - \delta_{8x}\right)^{2} + \left(\delta_{11y} - \delta_{8y}\right)^{2}} - \frac{b_{f}}{2} \end{cases}, & \text{bottom flange} \end{cases}$$

$$C = \max \left\{ \frac{\delta_{1y}}{\delta_{7y}} - \min \left\{ \frac{\delta_{8y}}{\delta_{14y}} \right\} \right\}$$
 (5)

Camber =
$$\frac{\delta_{1y} + \delta_{2y} + \delta_{3y} + \delta_{4y} + \delta_{5y} + \delta_{6y} + \delta_{7y}}{7}$$
 (6)

$$Sweep = \frac{\delta_{2x} + \delta_{6x} + \delta_{9x} + \delta_{13x}}{4}$$
 (7)

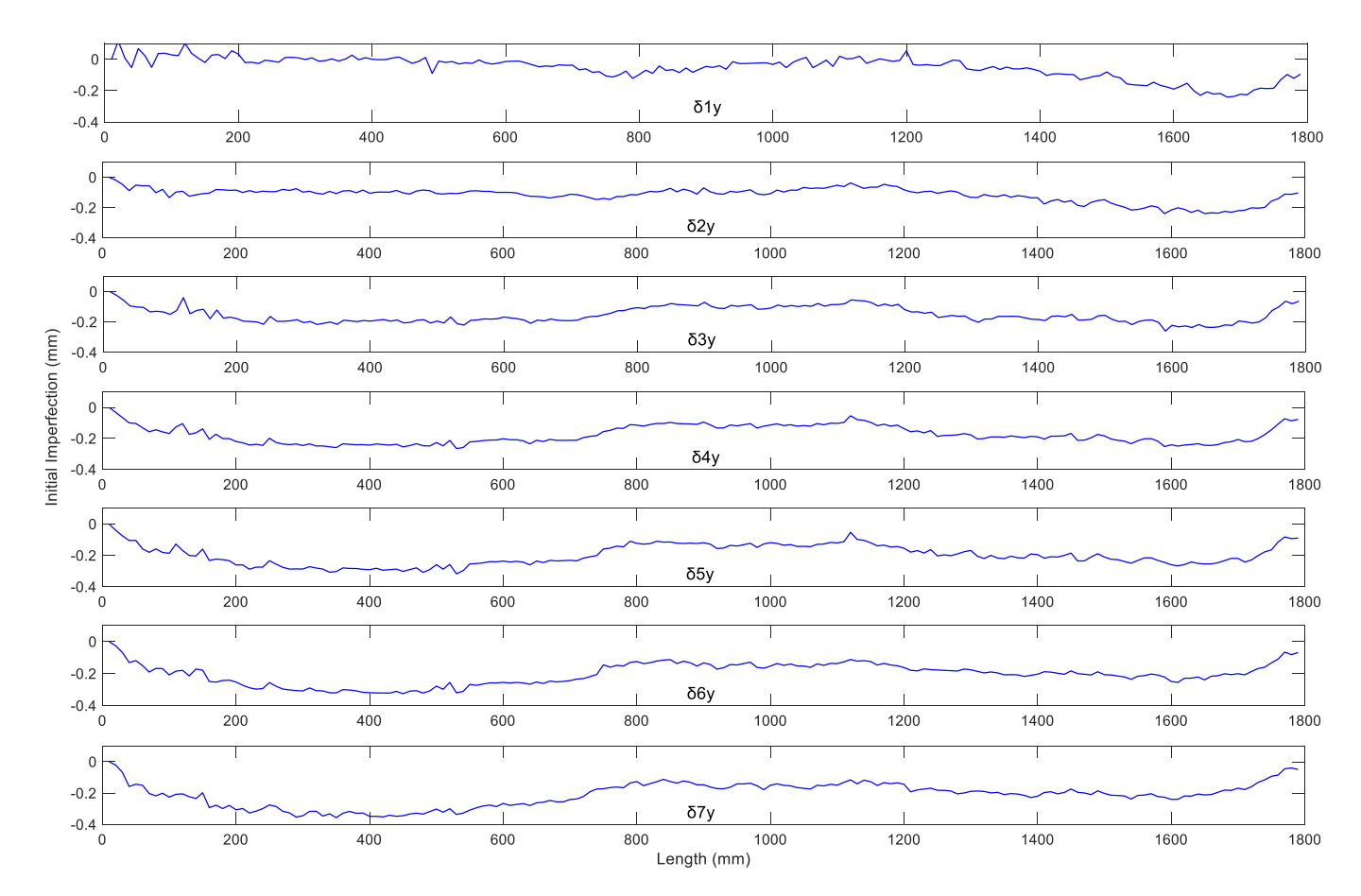


Fig. 5. Measured out-of-plane imperfection profile for top flange $(\delta_{1y}-\delta_{7y})$ in Specimen $150 \times 75-1$.

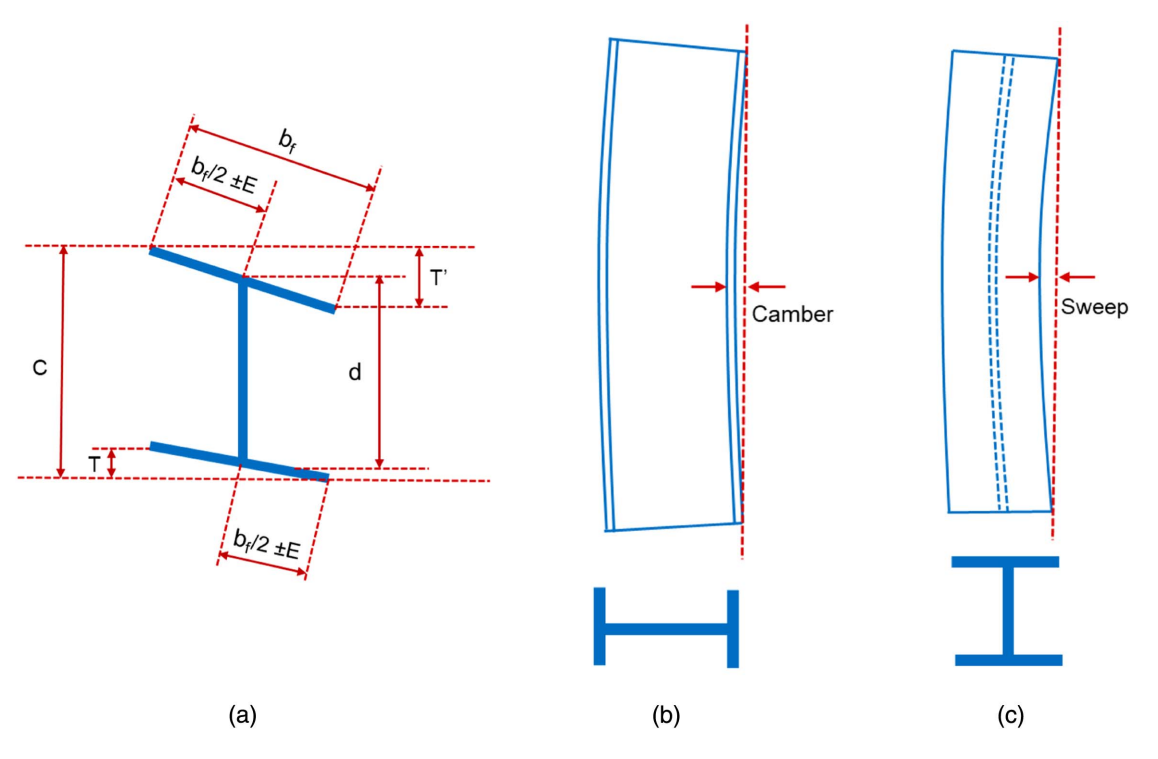


Fig. 6. Illustration of allowable (a) local cross-sectional; (b) in-plane global; and (c) out-of-plane global variations in W-shape members specified by ASTM (2019).

Table 2. Comparison of measured imperfections with permitted variations in W-shape members indicated in ASTM (2019) and CNS (2012)

Parameter	Mean (mm)	Maximum (mm)	Standard of deviation (mm)	Permitted (mm) [ASTM (2019)]	Permitted (mm) [CNS (2012)]
Δd	0.6	1.8	0.50	4.0	2.0
Δb_f	0.7	1.4	0.40	6.0	2.0
T + T'	1.1	2.5	0.70	6.0	Min of 0.02 b_f and 3.0
E	0.3	0.7	0.10	5.0	2.0
C	0.5	1.6	0.40	6.0	Max of 0.02 b_f and 3.0
Camber	0.2	0.4	0.07	1.8	1.8
Sweep	0.5	1.6	0.30	1.8	1.8

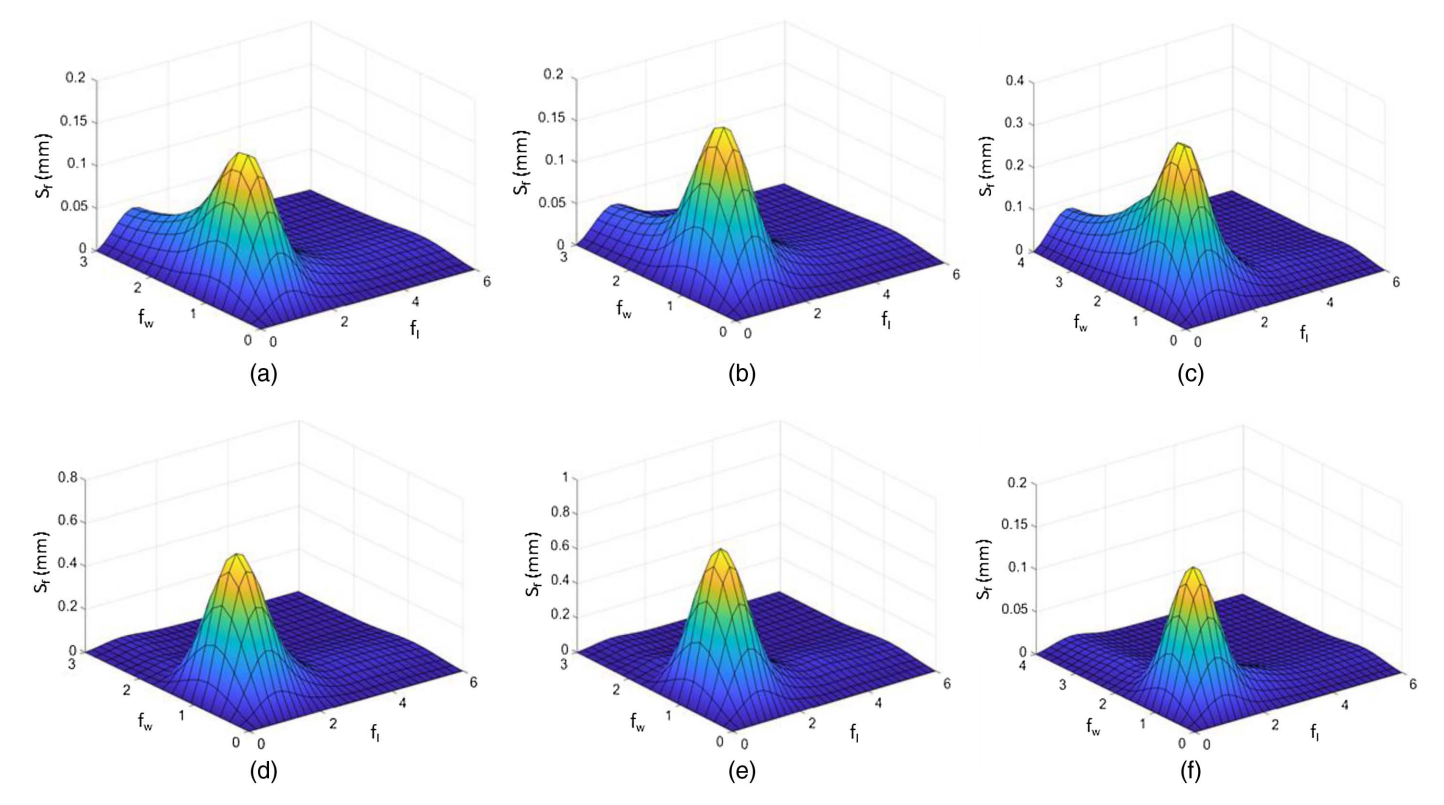


Fig. 7. Measured average 2D imperfection spectra of (a) out-of-plane profile of top flange; (b) out-of-plane profile of bottom flange; (c) out-of-plane profile of web; (d) in-plane profile of top flange; (e) in-plane profile of bottom flange; and (f) in-plane profile of web.

IGI Modeling

The traditional modal approach for modeling IGIs in W-shape members is a one-dimensional (1D) approach that superimposes a set of global and local buckling modes to create an imperfection field. The mode shapes are obtained from an elastic eigenvalue analysis and scaled such that the maximum deflection is equal to the manufacturing tolerances as discussed earlier. Although the traditional modal approach is quite convenient to implement, there is no evidence from actual measurements of IGIs in W-shape members to support this method, as demonstrated in Fig. 5.

A 2D random field spectral method, which considers the web and flange plates to be a random 2D field, is used for characterizing the measured IGIs. This method is more rational than the modal approach because it can explicitly account for the random nature of IGIs (Zeinoddini and Schafer 2012). Three separate elements of the W-shape cross section are considered: top flange, bottom flange, and web. The plates are assumed connected together at specific locations as shown in Fig. 4. The discrete 2D Fourier transform

(Bendat and Piersol 1971) is used to investigate periodicity in the measured imperfections using the following equation:

$$\begin{split} S_f(f_l,f_w) &= DFT(f_0(\hat{l},\hat{w})) \\ &= \frac{1}{N_1 N_2} \sum_{n_1=0}^{N_1-1} \left(e^{-2\pi i k_1 (n_1/N_1)} \sum_{n_2=0}^{N_2-1} e^{-2\pi i k_2 (n_2/N_2)} f_0(\hat{l},\hat{w}) \right) \end{split} \tag{8}$$

where f_0 = measured imperfection field; \hat{l} and \hat{w} = normalized location (with respect to the plate dimensions) on the 2D plates based on the axes shown in Fig. 4 (i.e., L and W); N_1 and N_2 = number of points (discretization) in each direction; f_l and f_w = imperfection frequencies in L and W directions, respectively; and k_1 and k_2 = wave numbers in each direction. It should be noted that f_l and f_w are dimensionless based on the fact that the transforms are evaluated using the normalized location (i.e., \hat{l} and \hat{w}) instead of the actual location (i.e., l and w). This approach is attributed to the fact that the measured specimens do not possess the same flange width.

The 2D transform provides information about the amplitude and frequency of the measured imperfection field. The dominant sine waves in the imperfection field are represented by the peaks in the transform. Despite the differences in the measured imperfection fields for the considered specimens, the 2D transforms have relatively similar shapes, with one or two peaks at low frequencies in both directions, followed by low to no content in higher frequencies. The consistent location of peaks in the 2D transforms reveal the existence of periodicity in the measured imperfection fields, which was also seen by Schafer and Peko (1998) in the 1D Fourier transform of the measured imperfection profiles in cold-formed members. Therefore, an average transform can be used to characterize the IGIs in W-shape members. The average transform for each imperfection profile (i.e., in-plane and out-of-plane) in each plate is obtained from the fourteen measured specimens as shown in Fig. 7.

The obtained 2D average transforms are termed *imperfection* spectrums following Schafer and Peko (1998), although they used the term in a 1D sense instead of the 2D application employed here. The imperfection spectrums can be used to generate new artificial imperfection distributions in the same way an earthquake response spectrum is used to synthesize artificial earthquake signals. More discussion about this type of generation can be found in the literature on random vibrations (Soong and Grigoriu 1993; Lin 1996), and specific discussions on this particular application (IGIs) can be found in Schafer and Peko (1998).

By modifying the 1D approach in Schafer and Peko (1998) to 2D, the imperfection signal can be expressed as

$$\begin{split} \hat{f}(\hat{l}, \hat{w}) &= \sum_{n_1=0}^{N_1-1} \sum_{n_2=0}^{N_2-1} \sigma_{n_1 n_2} (\mathbf{A}_{n_1 n_2} \cos(\omega_{n_1} \hat{l}) \cos(\omega_{n_2} \hat{w}) \\ &+ \mathbf{B}_{n_1 n_2} \sin(\omega_{n_1} \hat{l}) \cos(\omega_{n_2} \hat{w}) \\ &+ C_{n_1 n_2} \cos(\omega_{n_1} \hat{l}) \sin(\omega_{n_2} \hat{w}) \\ &+ D_{n_1 n_2} \sin(\omega_{n_1} \hat{l}) \sin(\omega_{n_2} \hat{w})) \end{split} \tag{9}$$

where $\hat{f}=$ generated imperfection signal; $\sigma_{n_1n_2}=$ square root of the volume under the n_1 , n_2 discretization of the imperfection spectrum; ω_{n_1} and ω_{n_2} = circular frequencies at the n_1 , n_2 discretization of the imperfection spectrum; and $A_{n_1n_2}$, $B_{n_1n_2}$, $C_{n_1n_2}$, and $D_{n_1n_2}$ = independent Gaussian random variables with zero mean and unit variance. The generated imperfection signal, which is sensitive to the number of discretizations (N_1 and N_2) and cutoff frequency in each direction (ω_{N_1} and ω_{N_2}), is normalized to have a unit maximum amplitude. N_1 , N_2 , ω_{N_1} , and ω_{N_2} are determined by the modeler. However, the quality of the generated signal with respect to the measured signals can be investigated by performing a 2D Fourier transform of the generated signals and comparing it to the imperfection spectrums shown in Fig. 7. It should also be noted that the proposed regeneration approach cuts the high-frequency noise imposed during the measurements, as was shown in the measured profile in Fig. 5.

Idealized IGI Spectrums

The average 2D imperfection spectrums shown in Fig. 7 are idealized based on the model defined by Eqs. (10)–(12), which are similar to those used for earthquake response spectrum analysis

$$S_{f}(f_{l}, f_{w}) = \min \begin{cases} S_{fl}(f_{l}) \\ S_{fw}(f_{w}) \end{cases}$$
 (10)

$$S_{fl}(f_l) = \begin{cases} a_1 f_l, f_l < f_{la} \\ a_1 f_{la}, f_{la} \le f_l \le f_{lb} \\ a_2 f_l^{-a_3}, f_l > f_{lb} \end{cases}$$
(11)

$$S_{fw}(f_w) = \begin{cases} a_4 f_w, f_w < f_{wa} \\ a_4 f_{wa}, f_{wa} \le f_w \le f_{wb} \\ a_5 f_w^{-a_6}, f_w > f_{wb} \end{cases}$$
(12)

The average imperfection spectrums are divided into three parts in the two primary directions (L and W) shown in Fig. 4: linear, constant, and descending power curves. The imperfection frequencies separating those parts are defined as f_{la} , f_{lb} , f_{wa} , and f_{wb} . S_f is the amplitude of the idealized 2D imperfection spectrum. S_{fl} and S_{fw} are the amplitudes of the idealized imperfection spectrums in the L and W directions, respectively. The parameters $a_1 - a_6$ are obtained using curve fitting for each part in each direction separately (Table 3). The resulting idealized imperfection spectrums are plotted in Fig. 8, with the coefficient of determination R^2 for the total curve shown on each plot. The average R^2 for the idealized curves is 0.855, which is deemed acceptable for such a complex idealization. The idealized imperfection spectrums can then be used to generate new normalized imperfection profiles for different W-shape members using Eq. (9).

The maximum amplitudes obtained from the measured results are first normalized to the thickness of each element (i.e., flange and web), which can be treated as a plate. This normalization is attributed to the difference between the web and flange thicknesses of the measured specimens. Then, the normalized values are used in a linear regression analysis to provide mathematical expressions to calculate the maximum amplitude in each direction for each of the three section elements. The imperfection profiles are scaled to the maximum amplitude in each direction. The flanges are assumed to have the same imperfection amplitude, but different profiles (i.e., different spectrums with the same amplitude expression). The maximum amplitudes are expressed as follows

$$\frac{\delta_{\text{max,out}_f}}{\mathsf{t}_f} = 0.00017 \frac{L}{r_{yf}} - 0.0093 \frac{b_f}{2t_f} \tag{13}$$

$$\frac{\delta_{\text{max,in}_f}}{t_f} = 0.00021 \frac{L}{r_{xf}} + 0.019 \frac{b_f}{2t_f}$$
 (14)

Table 3. Parameters of the proposed idealized 2D imperfection spectrums

		Coefficient								
Imperfection profile	f_{la}	f_{lb}	f_{wa}	f_{wb}	a_1 (mm)	a_2 (mm)	a_3	a_4 (mm)	<i>a</i> ₅ (mm)	a_6
Out-of-plane, top flange	0.80	1.29	0.80	1.15	0.20	0.30	2.37	0.20	0.21	1.61
Out-of-plane, bottom flange	0.90	1.29	0.80	1.06	0.21	0.35	2.31	0.24	0.22	1.83
Out-of-plane, web	0.95	1.21	0.90	1.15	0.39	0.60	2.13	0.41	0.46	1.29
In-plane, top flange	0.95	1.19	0.80	1.00	0.69	1.06	2.16	0.81	0.72	3.14
In-plane, bottom flange	0.95	1.19	0.75	1.02	0.89	1.38	2.34	1.13	0.97	3.28
In-plane, web	0.95	1.15	0.80	1.02	0.17	0.23	2.11	0.20	0.18	2.57

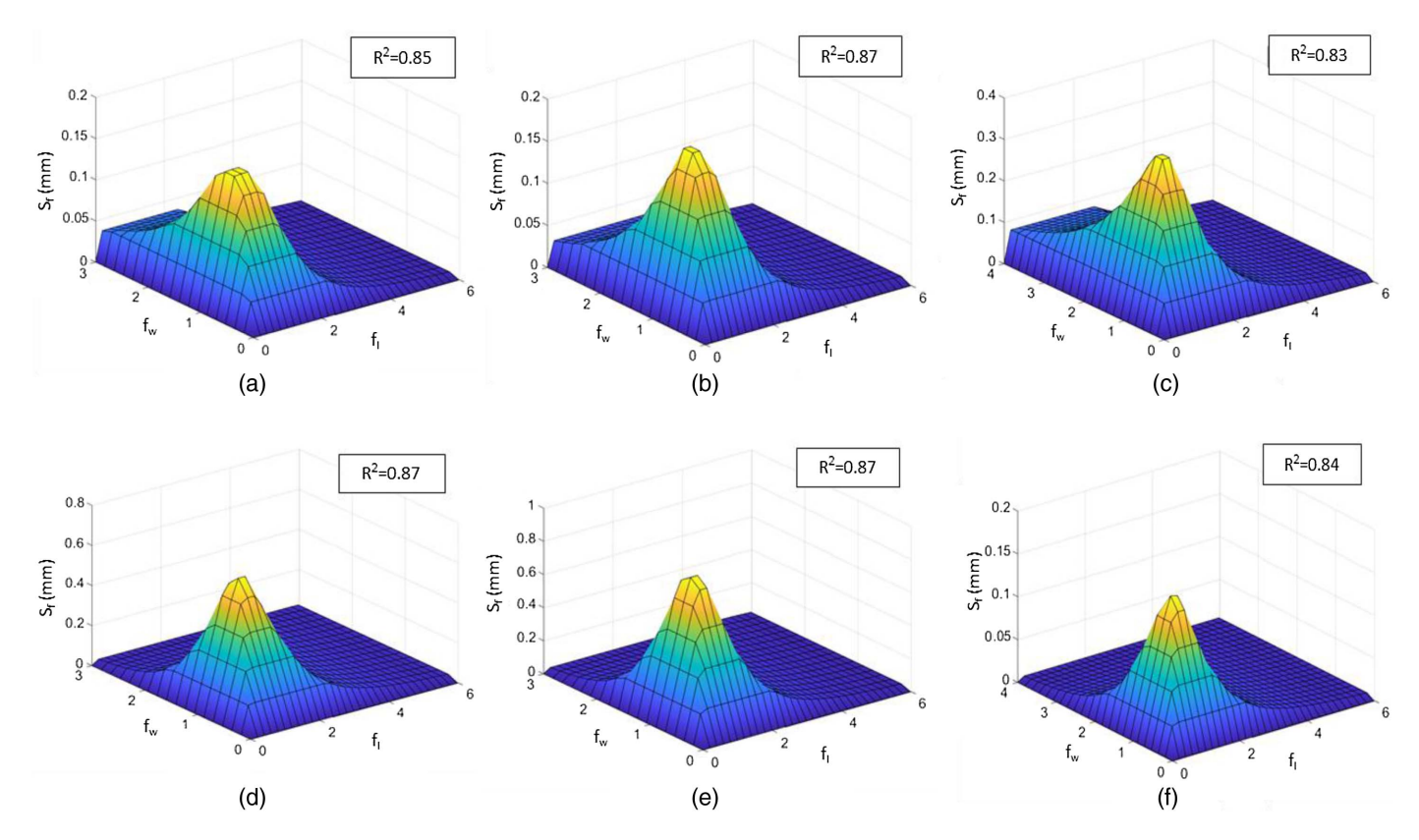


Fig. 8. Idealized 2D imperfection spectra for (a) out-of-plane profile of top flange; (b) out-of-plane profile of bottom flange; (c) out-of-plane profile of web; (d) in-plane profile of top flange; (e) in-plane profile of bottom flange; and (f) in-plane profile of web.

$$\frac{\delta_{\text{max,out}_w}}{t_w} = 0.0017 \frac{h}{t_w} + 5.51 \times 10^{-5} \frac{L}{r_{yw}}$$
 (15)

$$\frac{\delta_{\text{max,in}_w}}{t_w} = 0.00044 \frac{h}{t_w} + 0.00097 \frac{L}{r_{xw}}$$
 (16)

where $\delta_{\max, \text{out}_f}$ and $\delta_{\max, \text{in}_f}$ = maximum out-of-plane and in-plane imperfection amplitudes of the flange, respectively; $\delta_{\max, \text{out}_w}$ and $\delta_{\max, \text{in}_w}$ = maximum out-of-plane and in-plane imperfection amplitudes of the web, respectively; r_{yf} and r_{xf} = radius of gyration about the weak and strong axes of the flange plate, respectively; and r_{yw} and r_{xw} = radius of gyration about the weak and strong axes of the web plate, respectively. The coefficients of determination (R^2) of the proposed expressions are 0.80, 0.85, 0.93, and 0.85 for Eqs. (13)–(16), respectively.

Member-Level Computational Model Sensitivity to IGIs

Finite Element Modeling

The effect of incorporating IGIs in numerical models of individual column members subjected to combined axial and lateral loads is investigated. A total of sixteen columns with eight different W-shape sections (A992s teel) are selected to cover a wide range of local and global slenderness ratios (i.e., h/t_w , $b_f/2t_f$, and L/r_y), as can be seen in Fig. 1 and Table 4. The loading protocol consists of a force-controlled constant axial compressive load applied gradually for 2 s in simulation time and a displacement-controlled lateral load applied at the top of the column after the first 2 s in

simulation time. Three levels of constant axial compressive loads are investigated: $0.2P_y$, $0.3P_y$, and $0.4P_y$, where P_y is the axial yield capacity. The lateral load regime employs the cyclic ratcheting protocol designated CR2 in Wu et al. (2018a). The protocol was developed to represent the drift history at the top of first-story columns in a SMF during vertical progressive collapse due to an earthquake.

Detailed finite element models of the W-shape columns are created using the commercial software HyperMesh version 2017 and analyzed using the explicit solver of the general-purpose finite element software LS-DYNA version R7.0.0 as shown in Fig. 9.

Table 4. Properties of the studied W-shape columns

Section (in. × lb/ft)	h/t_w	$b_f/2t_f$	$L/r_{\rm y}$
W24 × 76	49.0	6.6	81.3
$W24 \times 76$	49.0	6.6	115.6
$W24 \times 84$	45.9	5.9	80.0
$W24 \times 84$	45.9	5.9	101.5
$W24 \times 335$	15.6	2.7	48.3
$W24 \times 335$	15.6	2.7	79.9
$W27 \times 161$	36.1	6.5	52.0
W27 × 161	36.1	6.5	70.6
$W27 \times 217$	28.7	4.7	50.6
$W27 \times 217$	28.7	4.7	70.5
$W30 \times 148$	41.6	4.4	78.9
$W30 \times 148$	41.6	4.4	100.0
$W30 \times 235$	32.2	5.0	51.3
$W30 \times 235$	32.2	5.0	80.3
$W30 \times 357$	21.6	3.5	49.5
W30 × 357	21.6	3.5	69.2

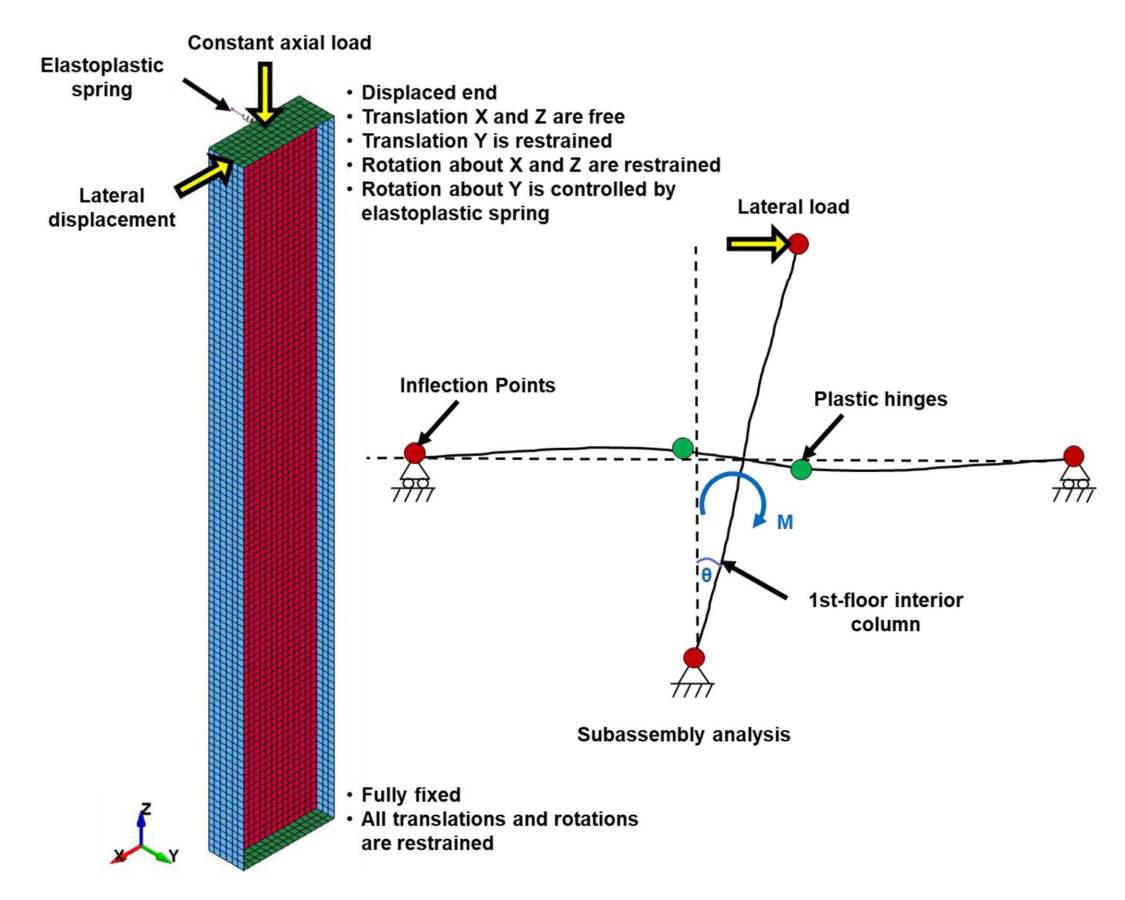


Fig. 9. Mesh and boundary conditions used in finite element models of studied columns.

The columns are discretized using fully integrated shell elements (ELFORM 16) based upon Mindlin–Reissner plate theory and formulated by Engelmann et al. (1989). The mesh size is the same as that used in Wu et al. (2018a), who conducted a mesh sensitivity study. A combined isotropic/kinematic hardening material model (MAT_153) developed by Huang and Mahin (2010) is assigned to the shell elements to capture the cyclic behavior of the studied column. The hardening parameters are calibrated to the true stress–true strain model by Arasaratnam et al. (2011) as done in Wu et al. (2018a). For all column models, the bottom end is assumed to be fully fixed, while in-plane rotation of the top end is restrained by an elastoplastic spring with properties determined by a subassembly analysis as shown in Fig. 9 (Wu et al. 2018a). The validation of the aforementioned modeling techniques can be seen in Fogarty et al. (2017), Wu et al. (2019), and Sediek et al. (2020a, b).

Simulations are conducted three times for each of the studied columns. The first simulation does not contain IGIs. The second employs IGIs as modeled by the traditional modal approach, where the global imperfection is assumed to be a sinusoidal shape with maximum amplitude similar to Elkady and Lignos (2018), i.e., L/1,500 at the midheight, while the local imperfections are based on the buckling modes specified by Elkady and Lignos (2018) from conventional buckling analysis with amplitudes of $b_f/250$ and h/250 for the flanges and web, respectively. The third has IGIs computed using the proposed random field spectral approach described earlier. The imperfection profile is generated randomly using Eq. (9) based on the average 2D imperfection spectrums shown in Fig. 7, and the maximum amplitude is evaluated using Eqs. (13)–(16). It should be noted that the generated imperfection field, being random, is based on one realization.

Constructing new imperfection fields will lead to different profiles and thus different simulation results.

Performance Parameters

Two performance parameters are used to quantitatively assess the effect of integrating IGIs using both approaches: ratio of maximum moment (RMM) and ratio of dissipated energy (RDE). RMM and RDE are defined as the ratios of the maximum end moment and dissipated energy of the imperfect column (i.e., traditional modal or proposed spectral) to that of the perfect column (i.e., no imperfection), respectively. Ratios less than unity imply a negative effect of IGIs on the behavior, i.e., IGIs degrade performance, as is commonly assumed, and vice versa.

Results and Discussion

The results with respect to the considered performance parameters, RMM and RDE, under different levels of initial axial load are listed in Table 5. The columns are designated as W-X-Y, where W is the W-shape profile, X is the global slenderness ratio (L/r_y) , and Y is the initial axial load ratio. For example, W24 × 84 × 80 – 20 is the W24 × 80 column with a global slenderness ratio of 80 subjected to an initial axial load of $0.2P_y$.

Effect of Local Slenderness Ratios

Figs. 10 and 11 plot the relationship between the slenderness ratios and performance parameters. Contrary to common assumption, it is evident that incorporating IGIs can sometimes lead to a positive effect on the performance of W-shape columns with respect to the perfect case (i.e., without incorporating IGIs) as shown by

Table 5. Summary of performance parameters

		$P/P_y = 0.2$			$P/P_y = 0.3$				$P/P_y = 0.4$				
		Traditional modal		Proposed spectral		Traditional modal		Proposed spectral		Traditional modal		Proposed spectral	
Section (in. \times lb/ft)	L/r_y	RMM	RDE	RMM	RDE	RMM	RDE	RMM	RDE	RMM	RDE	RMM	RDE
W24 × 76	81.3	0.95	0.97	1.05	1.00	0.95	1.04	1.02	1.00	0.89	0.96	1.00	1.02
$W24 \times 76$	115.6	1.03	0.96	1.05	0.93	1.06	1.27	0.99	1.16	1.05	1.04	1.02	1.10
$W24 \times 84$	80.0	0.91	1.05	0.95	1.01	0.88	0.95	0.99	0.84	0.93	1.11	0.93	0.93
$W24 \times 84$	101.5	0.98	0.95	1.01	0.93	0.96	0.99	0.98	0.96	0.92	1.15	0.90	1.00
$W24 \times 335$	48.3	1.00	0.97	1.00	1.01	0.97	0.97	0.98	0.97	0.95	1.01	0.95	1.03
$W24 \times 335$	79.9	0.99	0.90	1.02	0.93	1.02	0.96	0.98	0.93	0.98	1.00	1.00	0.98
$W27 \times 161$	52.0	0.92	0.90	0.95	0.93	0.92	0.89	0.98	0.92	0.92	0.90	0.98	0.93
W27 × 161	70.6	0.91	1.01	1.00	1.02	0.90	0.97	1.00	1.01	0.91	0.90	0.97	0.96
$W27 \times 217$	50.6	0.93	0.99	0.98	0.95	0.89	0.98	0.97	1.00	0.92	0.93	0.96	1.02
$W27 \times 217$	70.5	0.97	1.00	0.96	0.98	0.94	1.00	0.98	0.98	0.90	1.02	0.92	1.01
$W30 \times 148$	78.9	0.93	1.00	0.93	1.03	0.92	0.91	0.92	0.88	0.89	0.95	0.90	0.93
$W30 \times 148$	100.0	0.93	0.97	0.97	1.04	0.93	0.83	0.97	1.00	0.86	0.82	0.90	0.89
$W30 \times 235$	51.3	0.91	0.99	0.95	1.01	0.91	0.93	0.93	0.98	0.90	0.91	0.99	0.99
$W30 \times 235$	80.3	0.93	1.01	0.96	1.00	0.90	1.03	0.93	0.98	0.89	1.01	0.90	0.97
$W30 \times 357$	49.5	0.99	1.05	1.01	0.99	0.96	1.02	0.97	0.95	0.93	1.00	0.93	0.97
$W30 \times 357$	69.2	0.98	1.00	1.01	1.05	0.97	1.01	1.02	1.03	0.94	0.98	0.94	0.98
Minimum		0.91	0.90	0.93	0.93	0.88	0.83	0.92	0.84	0.86	0.82	0.90	0.89
Maximum		1.03	1.05	1.05	1.05	1.06	1.27	1.02	1.16	1.05	1.15	1.02	1.10
Average		0.95	0.98	0.99	0.99	0.94	0.98	0.98	0.97	0.92	0.98	0.95	0.98

the points above the unity lines in Figs. 10 and 11. It is also clear that there is a lot of scatter and no general positive or negative trend with respect to the slenderness ratios. This lack of consistency can be seen in the different directions of the trend lines of the plots. For example, compare W24×84-80-30 $(h/t_w=45.9, b_f/2t_f=5.9)$ and W24 × 76 – 115 – 30 ($h/t_w = 49$, $b_f/2t_f = 6.6$), which have similar local slenderness ratios (circled in Figs. 10 and 11). The traditional modal approach has a negative effect on both the maximum moment and dissipated energy of $W24 \times 84 - 80 - 30$ (RMM=0.88,RDE=0.95), while the effect is positive for W24 \times 76 - 115 - 30 (RMM = 1.06, RDE = 1.27). On the other hand, although the proposed spectral imperfection has a negative effect on the maximum moment for both columns (RMM = 0.99 for both columns), it has an inconsistent effect on the dissipated energy $(RDE = 0.84 \text{ and } 1.16 \text{ for } W24 \times 84 - 80 - 30 \text{ and } W24 \times 76 - 400 \text{ and } W24 \times 76 - 40$ 115 - 30, respectively). In general, the overall correlation between both approaches is weak. The average correlation coefficient between the results of both approaches is 0.54 and 0.56 for RMM and RDE, respectively.

Effect of IGI Randomness

Two representative columns are used to study the effect of randomness in the imperfection field: W30 × 357 – 50 – 30 ($h/t_w=21.6, b_f/2t_f=3.5$, a stocky Type I column as shown in Fig. 1) and W24 × 76 – 115 – 30 ($h/t_w=49, b_f/2t_f=6.6$, a slender Type II column as shown in Fig. 1). A total of 32 different imperfection profiles are randomly generated for each column model using the spectral approach. In addition, the effect of the sign of the global and local imperfections (i.e., positive or negative) in the traditional modal approach is considered through two additional models. Fig. 12 shows the computed moment-rotation behavior for the 32 spectral realizations, two modal cases, and the perfect column. Also shown in Fig. 12 are the deformed shapes (in the inserts) just before failure of the two columns. For the spectral case, the deformed shapes are for the two realizations with the largest and smallest peak moments.

Comparing Figs. 12(a and b) shows that in the latter load cycles, the more slender Type II column responses are more sensitive to the spectral imperfection profile than the stockier Type I column. The same sensitivity can also be seen in the modal approach. As shown in Fig. 12(a), the sign (positive or negative) of the predefined mode shape plays an important role in the effect of IGIs on the behavior of the Type II column. Assuming the imperfection in the positive out-of-plane direction (modal + ve) has a positive effect on the behavior of the Type II column (RMM = 1.06, RDE = 1.27). Assuming it in the negative out-of-plane direction (modal -ve) causes an opposite effect (RMM = 0.96, RDE = 0.85), significantly changing the performance parameters. In spite of these differences, the deformed shapes in the inserts in Figs. 12(a and b) indicate that the final failure mode is not affected by the randomness in the IGI approach or profile used.

An important conclusion from Fig. 12 is that the perfect column's response lies within the band of results for columns with various types of imperfections, supporting the notion that using a perfect column for simulation is a reasonable alternative to incorporating IGIs in this specific problem. This result is attributed to the small deformations that occur in the plastic hinge region in the early steps of the analysis of the perfect column. As the axial load is applied, the Poisson effect causes the web, which is constrained by the top and bottom plates, to bulge out slightly in the middle zone of the column, pushing out the flanges. Subsequent application of lateral loading causes further small deformations to occur in the early stages of the loading protocol. These deformations can be visualized in the highly magnified deformed shapes in Fig. 13 that show the plastic hinge region of W24 \times 76 \times 81 – 40 without IGIs at different stages in the analysis. The analysis platform must have sufficient numerical precision to capture these small deformations and promote geometric nonlinearity in subsequent phases of the response as shown in Fig. 13.

Effect of Axial Load

For both imperfection approaches, the influence of IGIs on the behavior of the studied columns increases with higher axial loads.

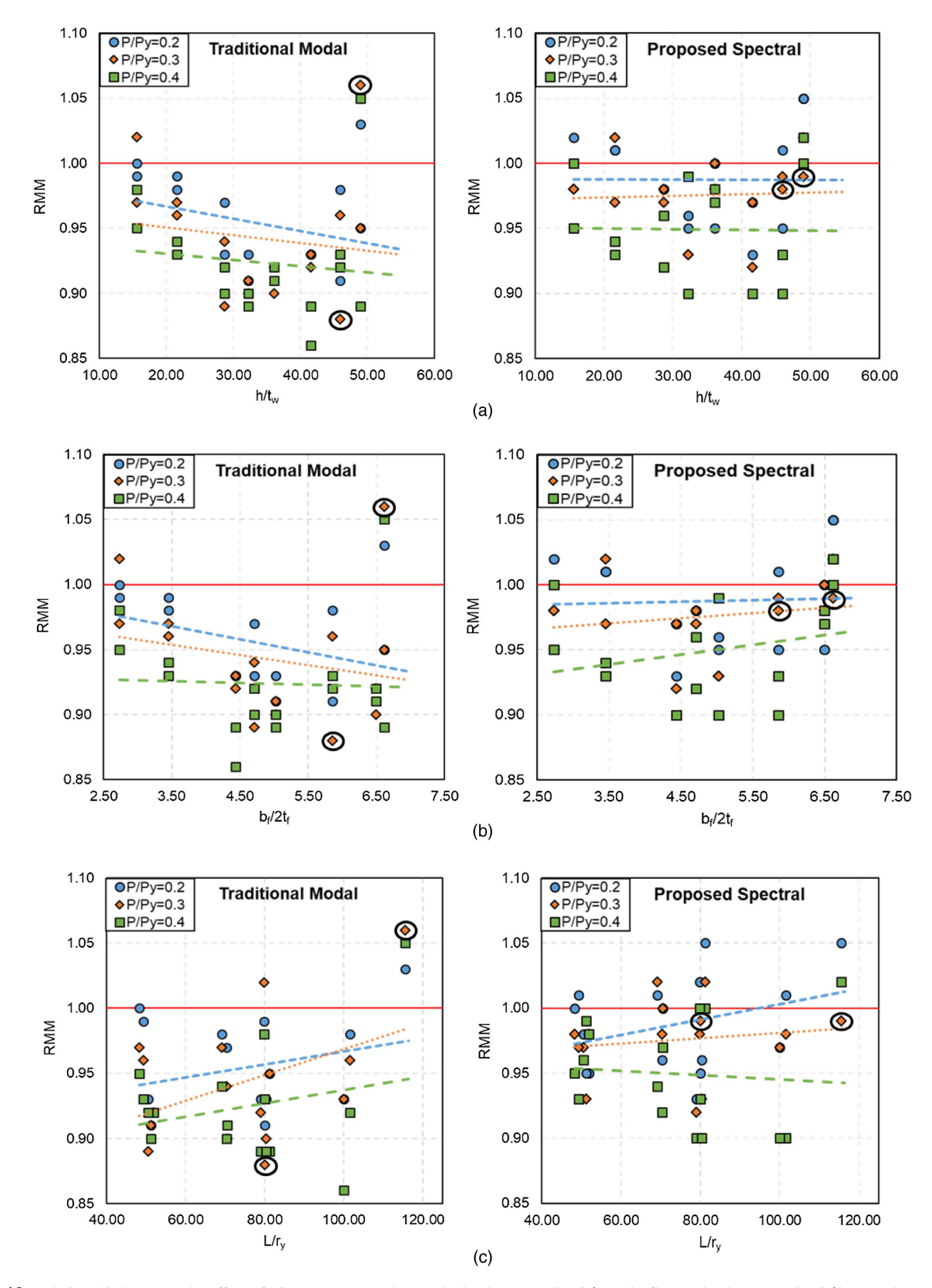


Fig. 10. Relationship between the effect of IGIs on RMM and (a) web slenderness ratio (h/t_w) ; (b) flange slenderness ratio $(b/2t_f)$; and (c) column global slenderness ratio (L/r_v) .

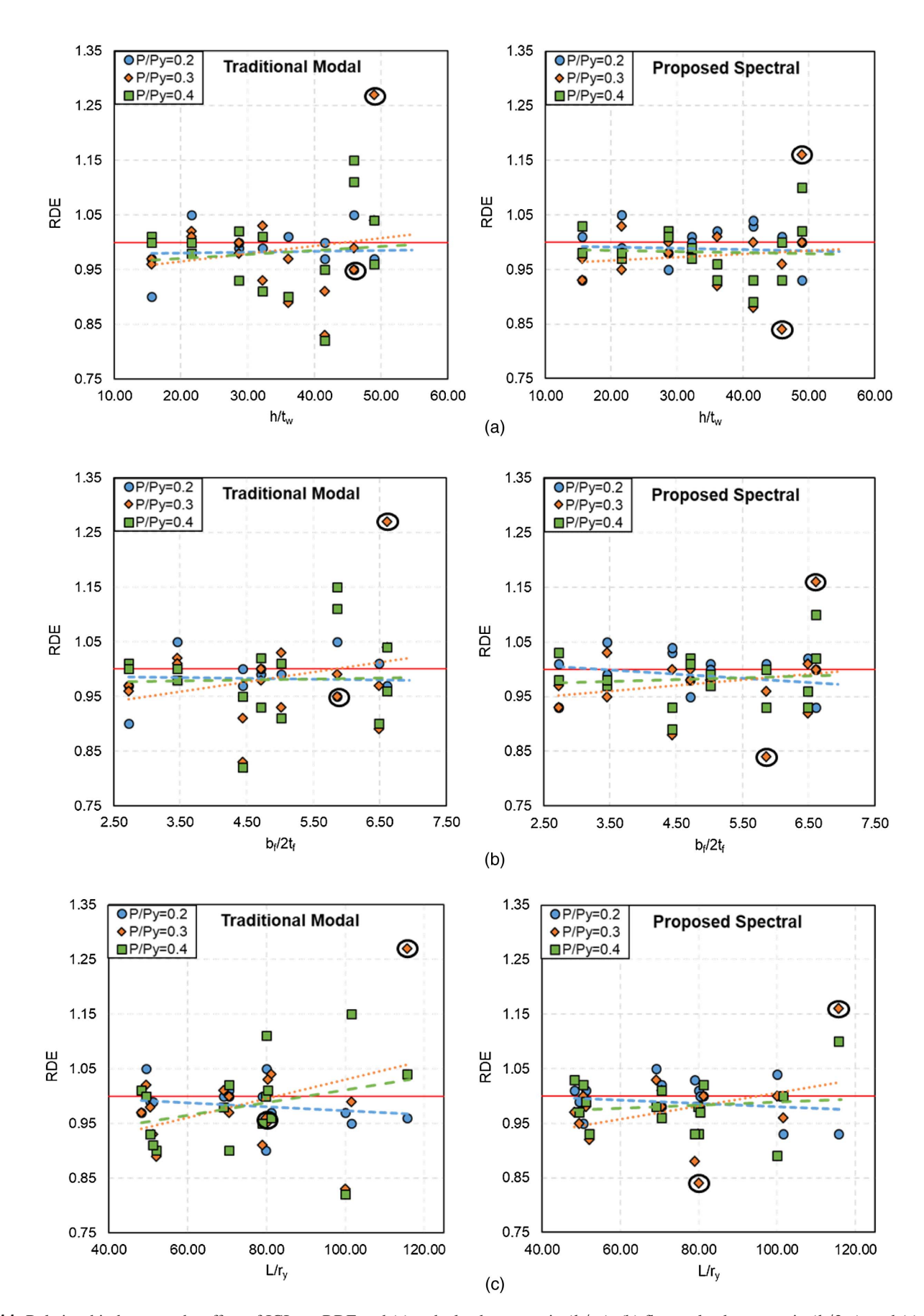
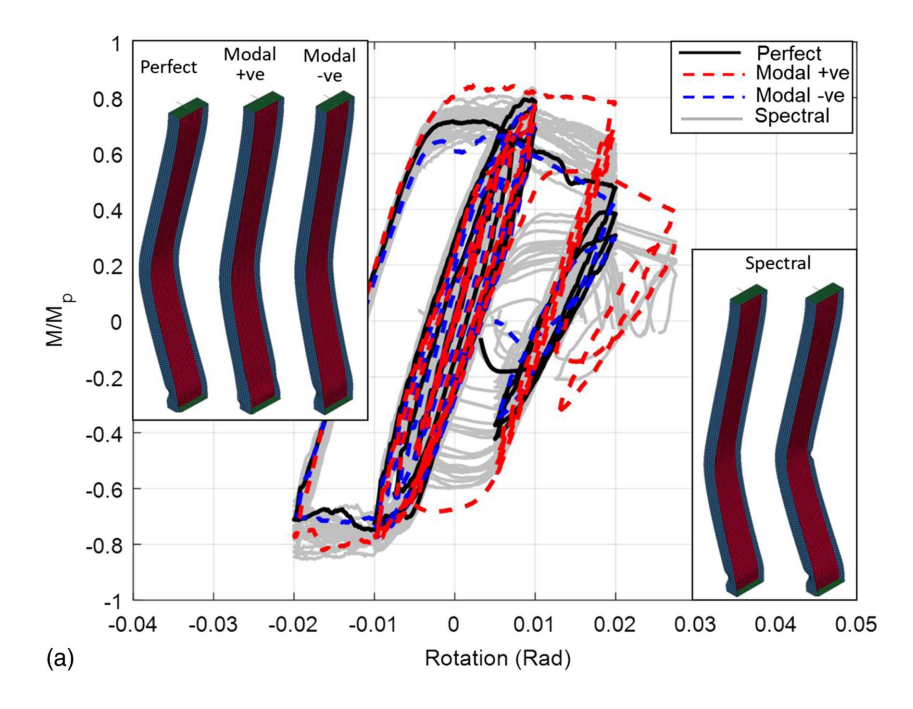


Fig. 11. Relationship between the effect of IGIs on RDE and (a) web slenderness ratio (h/t_w) ; (b) flange slenderness ratio $(b/2t_f)$; and (c) column global slenderness ratio (L/r_v) .



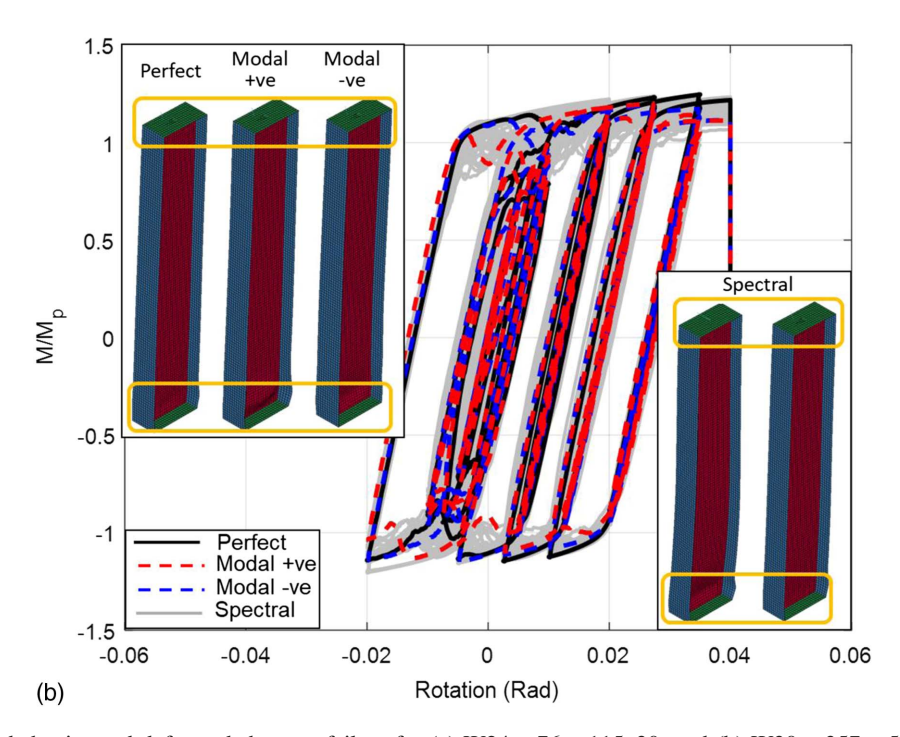


Fig. 12. Moment-rotation behavior and deformed shape at failure for (a) $W24 \times 76 \times 115-30$; and (b) $W30 \times 357 \times 50 - 30$ with different IGIs.

For example, on average between the two approaches, incorporating IGIs decreases the peak moment of W30 \times 148 - 100 $(h/t_w=36.1,b_f/2t_f=6.5)$ by 5%, 5%, and 12% when the initial axial load is $0.2P_y,0.3P_y$, and $0.4P_y$, respectively. It is evident that for a small axial load ratio of $0.2P_y$, the effect of including IGIs is small (-3% and -1.5% on average for RMM and RDE, respectively).

For all axial load ratios, the effect of including IGIs on RMM is relatively small, ranging from -14% to +6% with an average of -5%, as given in Table 5. However, the effect of including IGIs is more substantial on RDE (ranging from -18% to +27%), especially for slender columns (i.e., Type II columns in Fig. 1). This

difference is primarily attributed to the sensitivity of the last (failure) cycle to the assumed imperfection, as is clear in Fig. 12(a). However, the average effect is still small (-2%).

System-Level Computational Model Sensitivity to IGIs

Finite Element Modeling

The effect of IGIs on system-level behavior is studied through collapse assessment of four-story and eight-story steel SMFs.

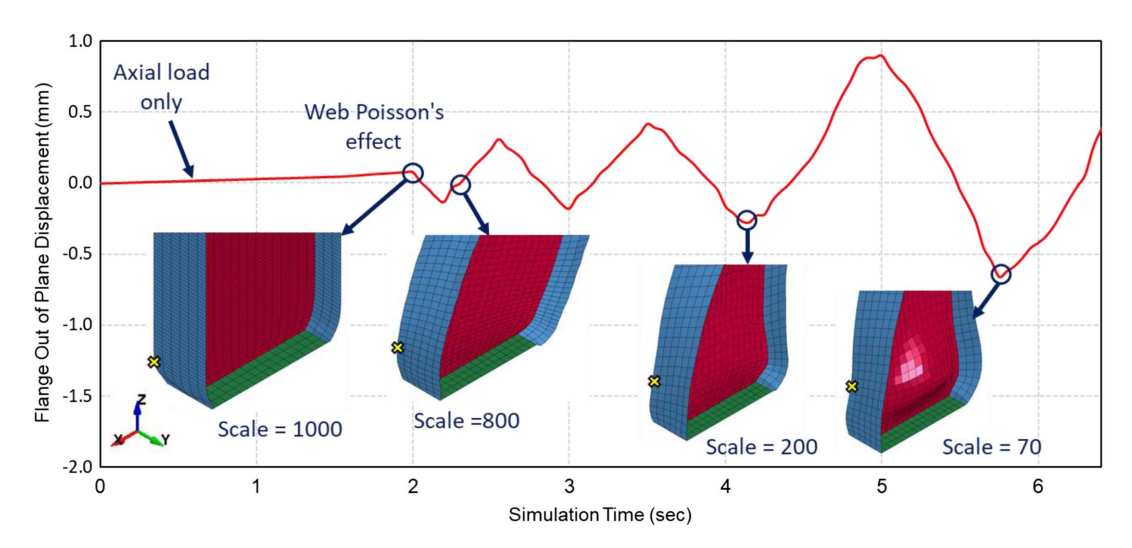


Fig. 13. Early out-of-plane displacements of flange of W24 \times 76 \times 81 - 40 without IGIs.

The frames have three bays with a span of 6.10 m and were designed by NIST (2010) for seismic design category D_{max} using W24 columns and reduced beam sections (RBS) per AISC (2016a, b) and ASCE (2016), as shown in Fig. 14. Details of the prototype frame can be found in Wu et al. (2018b). The frame models are fully fixed at their base and laterally braced to satisfy the requirements for highly ductile members in the AISC Seismic Provisions (AISC 2016b). Systemwide P-Delta effects are considered by connecting a leaning column to the SMF with rigid truss members, as shown in Figs. 14(b and c). A gravity load equal to half of the building floor mass minus that distributed to the SMF system is applied at each floor of the leaning column. The initial axial load ratios, P/P_{v} , for the first-story exterior columns of four-story and eightstory SMFs under distributed gravity load are 0.18 and 0.27, respectively. To investigate the effect of IGIs under higher axial load, an additional four-story frame with increased gravity load that results in $P/P_v = 0.27$ is used. A mass-proportional damping of 2.5% was assumed at the first mode period of the SMFs. The four-story and eight-story SMFs are discretized using approximately 96,000 and 235,000 elements, respectively, as done for the individual columns discussed earlier, and modeled with and without IGIs.

Seven different conditions of IGIs are considered: (1) P (perfect): no IGIs; (2) G (global): contains a global imperfection of a sinusoidal shape with a maximum amplitude of (L/1,500) at the midheight for all columns; (3) GA (global amplified): similar to G, but with a maximum amplitude of (L/1,000); (4) GL1 (global-local at first story): in addition to Condition 2, contains local imperfections from conventional buckling analysis with amplitudes of $b_f/250$ and h/250 for the flanges and web, respectively, for the first-story columns; (5) GOL1 (global opposite-local at first story): similar to GL1, but contains global imperfection with an opposite direction to the one applied to GL1; (6) GLA (global-local at all stories): similar to GL1, but contains local imperfection for all columns; and (7) S (spectral): contains IGIs generated by the average 2D imperfection spectrums [Fig. 7 and Eqs. (6)–(9)] for all columns. Except GOL1, the geometric imperfections in frames with IGIs computed using the traditional modal approach, i.e., G, GA, GL1, and GLA, are applied in the same direction.

The collapse capacity of the frame is evaluated using eleven ground motion records selected from the far-field record set in FEMA P695 (FEMA 2009). As detailed in Wu et al. (2018b), while vertical progressive collapse can be directly detected from the deformed shape of the frame, sidesway collapse is determined by two

collapse criteria: (1) maximum story drift ratio exceeding 10%; and (2) an increase of 2% or more in story drift ratio during the 10-s window immediately after the time needed for the Arias intensity to reach 95% ($t_{IA=95\%}$) (Arias 1970). Based on the aforementioned collapse criteria, incremental dynamic analysis (IDA) (Vamvatsikos and Cornell 2002) is applied to obtain two collapse parameters associated with each record: spectral acceleration and maximum story drift ratio at frame collapse, $S_{a,C}(T_1,5\%)$ and SDR_{max,C}, where T_1 (= 1.67 and 2.37 s for the four-story and eight-story frames, respectively) is the fundamental period of the SMFs. The collapse fragility curves of each frame are then constructed using the median value ($S_{a,C}$ and SDR_{max,C}) and dispersion (β_{Sa} and β_{SDR}) of the two parameter sets.

Results and Discussion

In order to facilitate discussion of the key parameters, a descriptive naming scheme is used for the frames. For example, S4-18-P is a four-story frame without IGIs under gravity load that results in an initial axial load of $0.18P_y$ for first-story exterior columns, whereas S8-27-S is an eight-story frame with IGIs generated by the spectral approach and an initial axial load of $0.27P_y$ in its first-story exterior columns.

The collapse fragility curves of the four-story and eight-story frames are shown in Figs. 15 and 16, respectively, with the median values and dispersions listed in Table 6. As can be seen in Fig. 15(a), the collapse fragility curves with spectral acceleration along the x-axis for the S4-18 frames, i.e., the four-story frames with $P/P_y=0.18$ for first-story exterior columns, are almost identical, suggesting that the effect of IGIs on the collapse capacity of the S4-18 frames is negligible. The IGIs can be more influential with increased magnitude (i.e., S4-18-GA), but the $S_{a,C}(T_1,5\%)$ of the S4-18 frames are still quite close to each other under most ground motion records except records Landers/YER270 and Northr/MUL009. The effect of IGIs under Landers/YER270 is more obvious due to the weaving behavior [where the frame suffers from smaller response at a higher spectral acceleration (Vamvatsikos and Cornell 2002)] that occurs in S4-18-P prior to collapse.

For record Northr/MUL009, the reason for the more pronounced effect is the alignment between the deformed shape of the buckled column in S4-18-P and the applied global IGI, which exacerbates the buckling behavior. On the other hand, the global imperfection may have a positive effect if its direction is opposite to that of the

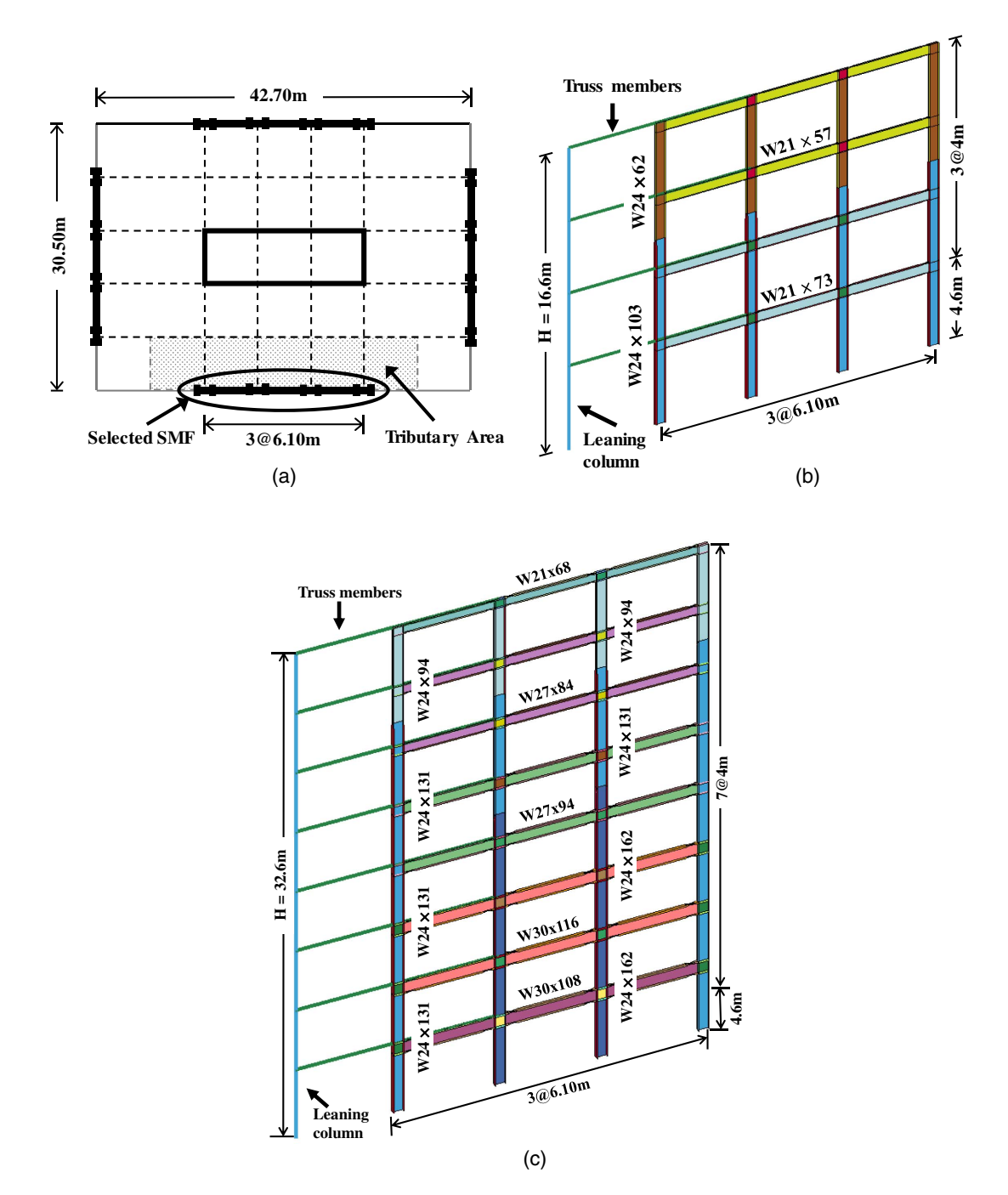


Fig. 14. (a) Plan configuration; (b) finite element model of the four-story SMF; and (c) finite element model of the eight-story SMF.

column buckling shapes in S4-18-P. For example, under record Impvall/H-DLT262, $S_{a,C}(T_1,5\%)$ is slightly increased because the columns in S4-18-G are forced to buckle differently than the columns in S4-18-P due to misaligned global imperfections, as shown in Figs. 17(a and b). This phenomenon is more evident in S4-27-P. By applying the GL1 condition to S4-27-P, the $S_{a,C}(T_1,5\%)$ of the S4-27 frame increases because of the consistency of the column buckling shapes and frame collapse mechanisms among ground motion records. However, the increase of 3% is still small, even though the S4-27 frame is dominated by vertical progressive collapse due to early global buckling of the columns.

The effect of local IGIs on $S_{a,C}(T_1, 5\%)$ is mostly negative and therefore more consistent than global IGIs. While the detailed simulation results are not shown, adding L1 (local at first story) IGIs to

S4-18-G and S8-27-G has a positive effect on only three and one of eleven records, respectively. Adding LA is even more significant. This result can be extrapolated from the exacerbated local buckling behavior shown in Fig. 18(b). Nevertheless, the resulting effect of local IGIs on $S_{a,C}(T_1,5\%)$ is still small, and only 4% even for the S8-27 frame (comparing S8-27-GL1 to S8-27-G), which failed by sidesway collapse due to component deterioration, as can be seen in Table 6.

The effect of IGIs by the proposed spectral approach, i.e., S4-18-S and S8-27-S, is the most inconsistent due to its random nature. Applying such IGIs can even slightly increase $S_{a,C}(T_1,5\%)$ for S4-18-S, as seen in six of the ground motion records. As a result, the S condition is the least influential on frame collapse behavior among the IGI options considered.

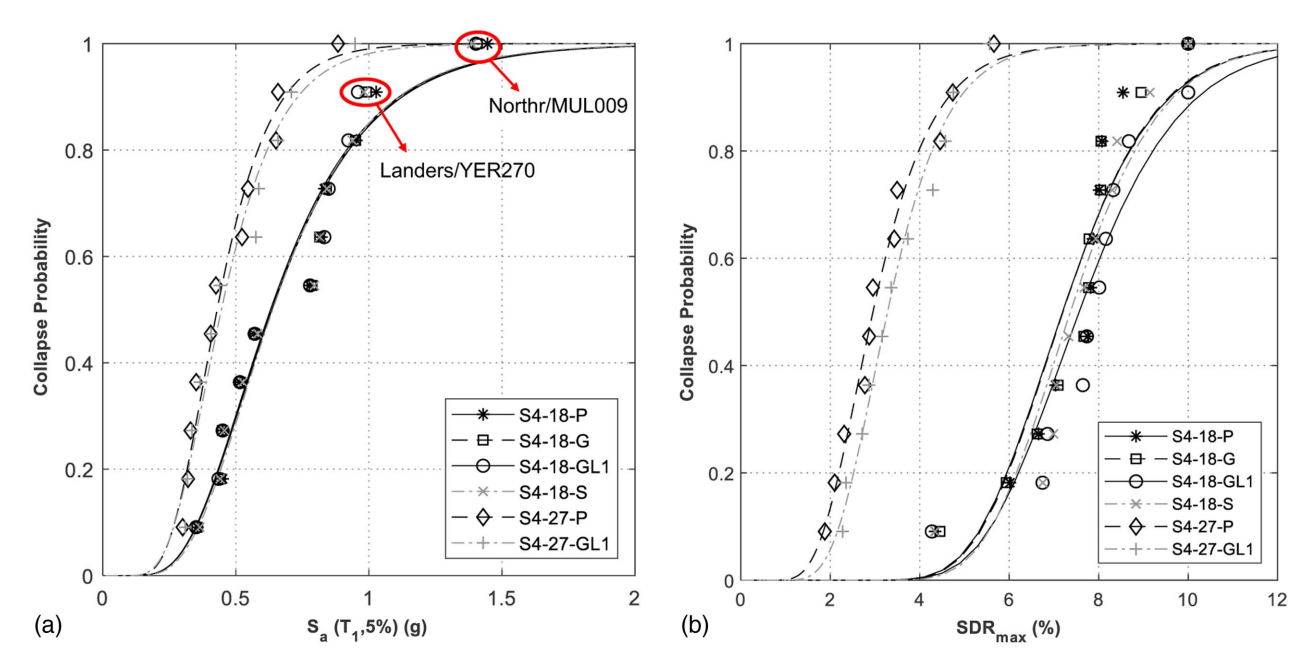


Fig. 15. Collapse fragility curves of the four-story SMFs with (a) spectral acceleration $S_a(T_1, 5\%)$; and (b) maximum story drift ratio SDR_{max} along x-axis.

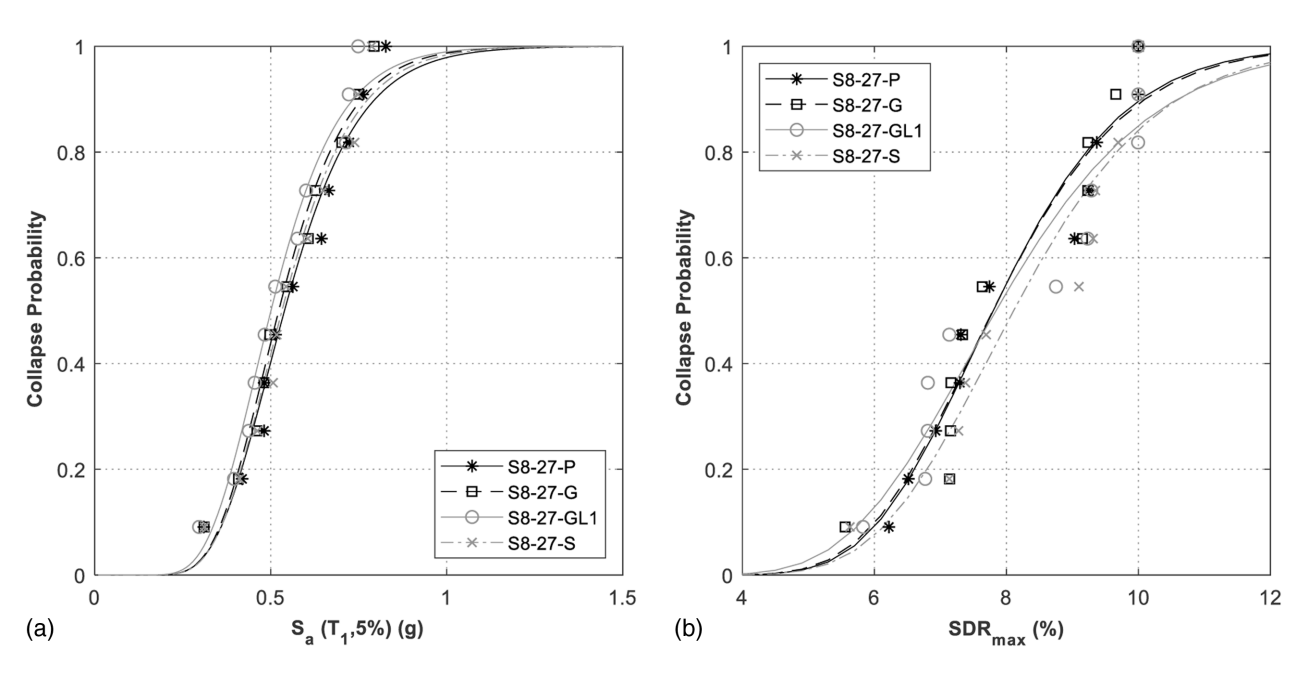


Fig. 16. Collapse fragility curves of the eight-story SMFs with (a) spectral acceleration $S_a(T_1, 5\%)$; and (b) maximum story drift ratio SDR_{max} along *x*-axis.

Considering ductility, the effect of IGI is also inconsistent under different ground motion records, but more significant than when considering the influence on spectral acceleration, as shown in Figs. 15(b) and 16(b). Under the same record, $\mathrm{SDR}_{\mathrm{max},C}$ has a larger variation among the frames than $S_{a,C}(T_1,5\%)$. However, unlike $S_{a,C}(T_1,5\%)$, $\mathrm{SDR}_{\mathrm{max},C}$ always increases when IGIs are applied, except for GOL1, which greatly reduces the $\mathrm{SDR}_{\mathrm{max},C}$ of one ground motion record, triggering vertical collapse for the four-story frame due to directional alignment between the deformed shape of the buckled column and the applied global IGI. The increase of $\mathrm{SDR}_{\mathrm{max},C}$ results from the amplified story drifts

due to IGIs under the same spectral acceleration of each record. As the change in $S_{a,C}(T_1,5\%)$ of each record is minimal, the resulting SDR_{max,C} is slightly increased. Although this increase in drift is small, it sometimes leads to a shift in the collapse mode. For example, with comparable $S_{a,C}(T_1,5\%)$, the collapse modes of S4-18-P and S4-18-GL1 under record Impvall/H-DLT262 are vertical and sidesway collapse, respectively. The frame collapses are both initiated by buckling of a first-story exterior column but are followed by subsequent buckling of adjacent columns and compromised lateral resistance due to P-Delta effects, respectively, as shown in Fig. 19.

Table 6. Collapse assessment results of the SMFs with different imperfection conditions

Frame						No. of records		
identifier	$\tilde{S}_{a,C}(T_1,5\%)$ (g)	β_{Sa}	$\widetilde{SDR}_{max,C}$ (%)	$\beta_{\rm SDR}$	SC	VC		
S4-18-P	0.636	0.45	7.19	0.23	9	2		
S4-18-G	0.634	0.44	7.20	0.22	9	2		
S4-18-GA	0.629	0.44	7.32	0.23	9	2		
S4-18-GL1	0.630	0.44	7.56	0.23	10	1		
S4-18-GOL1	0.624	0.44	6.88	0.32	9	2		
S4-18-GLA	0.624	0.44	7.34	0.21	9	2		
S4-18-S	0.639	0.43	7.37	0.21	9	2		
S4-27-P	0.430	0.36	2.95	0.35	0	11		
S4-27-GL1	0.444	0.39	3.28	0.31	0	11		
S8-27-P	0.539	0.30	7.80	0.20	11	0		
S8-27-G	0.523	0.29	7.79	0.20	11	0		
S8-27-GL1	0.500	0.30	7.84	0.24	11	0		
S8-27-S	0.532	0.30	8.11	0.21	11	0		

Note: SC = sidesway collapse; and VC = vertical collapse.

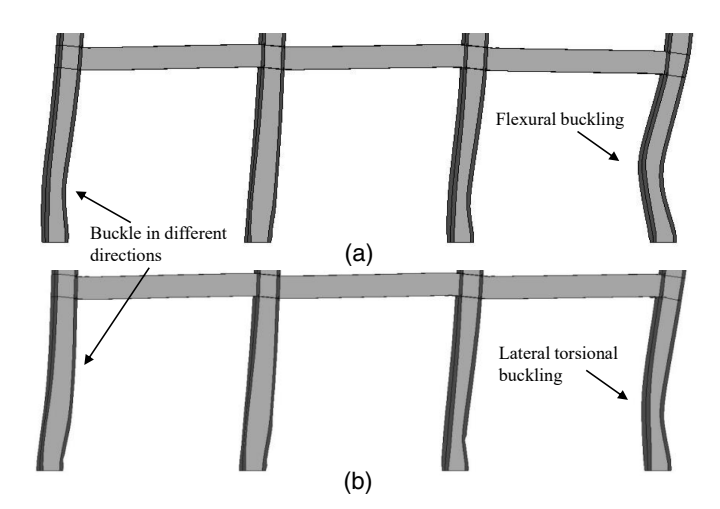


Fig. 17. Deformed shapes of first-story columns at collapse under ground motion record Impvall/H-DLT262 (a) S4-18-P; and (b) S4-18-G.

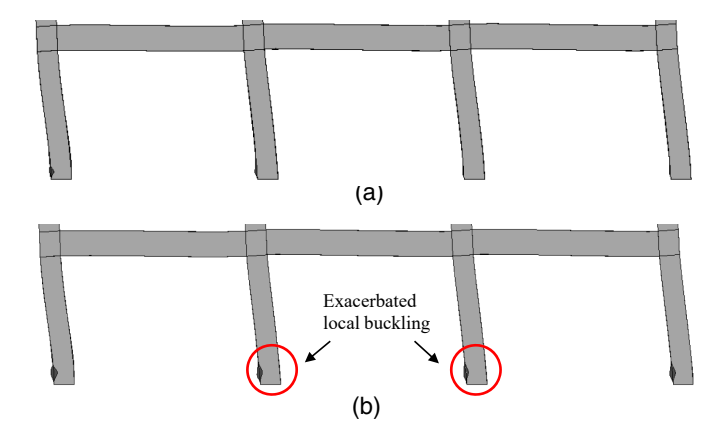


Fig. 18. Deformed shapes of first-story columns at collapse under ground motion record Kobe/SHI000 (a) S8-27-G; and (b) S8-27-GL1.

Overall, the effect of initial geometric imperfection is quite small for the studied frames. It also depends on the buckling shapes and collapse mechanisms in a perfect frame, as well as ground motion records. Column section properties also play a role. For example, the effect of global and local imperfections is more obvious in S4-27-P and S8-27-P with different failure mechanisms due to high and low slenderness ratios (i.e., L/r_v and h/t_w) of the first-story columns, respectively, as discussed before. The effect of IGIs increases with the increase of initial axial load, P/P_v . However, the resulting changes in $S_{a,C}(T_1,5\%)$ of the considered frames range only between -2% and +0.5% and between -7% and +3% when $P/P_v = 0.18$ and 0.27 for first-story exterior columns, respectively. This finding is consistent with the results from the member-level study. As a result, even though the IGIs and their direction can change the column buckling behavior as well as the frame collapse mode in certain situations, as highlighted in Figs. 17-19, their influence on frame collapse capacity is marginal and uncertain unless a perfect frame is also assessed.

Practical Implications and Limitations of This Work

This paper addresses the specific case of steel W-shape columns subject to combined axial and lateral loading through member-level studies and their use in SMFs. The simulation results show that the effect of incorporating IGIs is small [on average, -4.5% and -2%for RMM and RDE, respectively, and -1.4% for $S_{a,C}(T_1, 5\%)$] when the axial load level is limited to $0.4P_{y}$, which is rarely exceeded in earthquake engineering practice. Given the limited effect of IGIs in these situations and, more fundamentally, the random nature of IGIs and their inconsistent effect, analysts need not incorporate IGIs into their models. However, the analysis platform must have sufficient numerical precision to capture the small deformations that occur in the early steps of the analysis due to the applied loads and boundary conditions and promote geometric nonlinearity in subsequent phases of the response as shown earlier in Fig. 13. The modeling approaches described earlier and in Sediek et al. (2020a) are examples of the type of analysis that can be used. For different modeling schemes, proper experimental validation and sensitivity studies are essential to ensure that appropriate results can be obtained.

If IGIs must be included in an analysis, and given that the overall effect of IGIs is small and inconsistent between both studied methods, either the proposed spectral approach or modal method may be used. The probabilistic nature of the former makes it possible to simulate a range of responses to bracket the likely behavior of a steel member as shown in Fig. 12. For both methods, realistic values for the peak amplitudes should be used [e.g., Eqs. (13)–(16)]. Arbitrary selection of calibration parameters such as IGI amplitudes, number of mode shapes used, and their direction to more accurately fit test results may inadvertently mask the effects of initial stresses or boundary constraints, providing false confidence during validation studies.

A limitation of this work is that the measurements were completed on only fourteen specimens and the computational results were gleaned from a limited range of members. Additional research is needed to consider a broader set of W-shape members in order to generalize the results obtained. Columns that are part of fabricated subassemblages should also be considered because the fabrication process may introduce additional IGIs. A further limitation of this work is that the proposed spectral approach ignores the correlation between the six 2D random fields, which may affect the generated imperfection profiles.

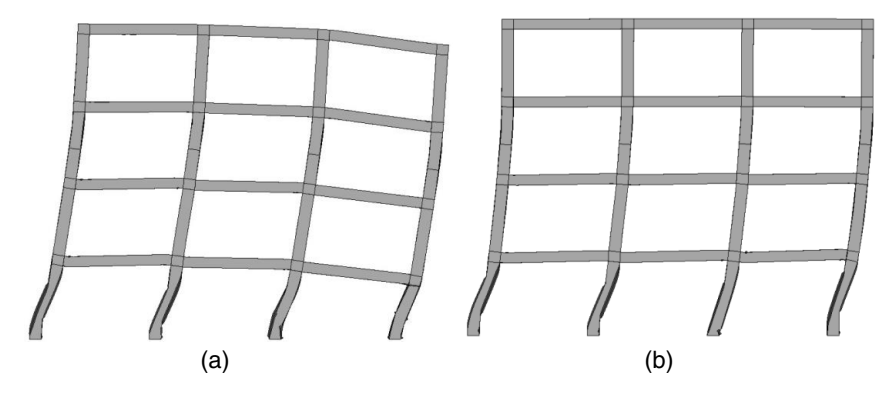


Fig. 19. Collapse mechanism of (a) S4-18-P; and (b) S4-18-GL1 under ground motion record Impvall/H-DLT262.

Summary and Conclusions

The IGIs in steel W-shape members were measured using a 3D noncontact laser-scanning technique. A spectral approach that models the IGIs in each plate of the W-shape member as a 2D random field, which is commonly used to model random vibrations, was used to characterize the measured IGIs. The 2D Fourier transforms of the measured IGI profiles revealed the existence of periodicity in the measured fields. Therefore, the average 2D Fourier transforms of the measured IGI profiles were used to introduce the concept of idealized imperfection spectrums that could be used to generate new normalized IGI profiles (i.e., having a unit maximum amplitude) for different specimens based on actual imperfection data. The measured data was used in a regression analysis to propose expressions for the maximum amplitude of IGIs in W-shape steel members.

Although the traditional modal approach for modeling IGIs is convenient to use, the assumed IGI shapes do not match well with the measured fields. Therefore, the modal method and the proposed spectral approach were used to study the sensitivity of computational models to both approaches at the member and system levels. It was shown that there was weak correlation between both approaches, and that in a few situations, column buckling behavior as well as frame collapse modes were influenced by the approach taken. However, the general effects of IGIs from both methods were inconsistent and quite small, within 3% on average, for initial axial load levels of P/P_{ν} of 0.4 and 0.27 at the member- and system level, respectively. Based on this finding, it was recommended that IGIs need not be incorporated in high-fidelity numerical models of W-shape members subjected to combined axial and cyclic lateral loads. This was conditioned upon the use of an analysis platform with sufficient numerical precision to capture early small deformations that promote geometric nonlinearity in the response. This result is of significance because introducing IGIs can be a timeconsuming endeavor for system-level studies, depending on the approach taken and complexity of the structure.

Data Availability Statement

All data, models, and code generated or used during the study appear in the published article.

Acknowledgments

This work was jointly supported by the National Taiwan University within the framework of the Higher Education Sprout Project by

the Ministry of Education (MOE) in Taiwan, Grant Nos. 108L8806 and 109L8836, the US National Science Foundation (NSF) through Grant ACI-1638186, and the US Department of Commerce, National Institute of Standards and Technology, Award 70NANB171TZ91. Any opinions, findings, conclusions, and recommendations expressed in this paper are those of the authors and do not necessarily reflect the views of the sponsors.

References

AISC. 2016a. Code of standard practice of steel buildings and bridges. ANSI/AISC 303-16. Chicago: AISC.

AISC. 2016b. Seismic provisions for structural steel buildings. ANSI/AISC 341. Chicago: AISC.

Almutairi, T., K. Naudi, N. Nairn, X. Ju, J. Whitters, and A. Ayoub. 2018. "Replacement of the distorted dentition of the cone-beam computed tomography scans for orthognathic surgery planning." *J. Oral Maxillofacial Surg.* 76 (7): 1–8. https://doi.org/10.1016/j.joms.2018.02.018.

Arasaratnam, P., K. S. Sivakumaran, and M. J. Tait. 2011. "True stress-true strain models for structural steel elements." *ISRN Civ. Eng.* 1–11. https://doi.org/10.5402/2011/656401.

Arias, A. 1970. "A measure of earthquake intensity." In Seismic design for nuclear power plants, edited by R. J. Hansen, 438–483. Cambridge, MA: MIT Press.

ASCE. 2016. Minimum design loads for buildings and other structures. ASCE/SEI 7. Reston, VA: ASCE.

ASTM. 2019. Standard specification for general requirements for rolled structural steel bars, plates, shapes, and sheet piling. ASTM A6/A6M. West Conshohocken, PA: ASTM.

AutoDesk. 2018. *User's guide-AutoCAD 2018*. San Rafael, CA: Autodesk. Bendat, J. S., and A. G. Piersol. 1971. *Random data: Analysis and measurement procedure*. New York: Wiley.

CNS (National Standards of the Republic of China). 2012. *Dimensions, mass and permissible variations of hot rolled steel sections*. CNS 1490 G1011. Taipei, Taiwan: Bureau of Standards, Metrology and Inspection.

Cravero, J., A. Elkady, and D. G. Lignos. 2020. "Experimental evaluation and numerical modeling of wide-flange steel columns subjected to constant and variable axial load coupled with lateral drift demands." *J. Struct. Eng.* 360 (3): 1–19. https://doi.org/10.1061/(ASCE)ST .1943-541X.0002499.

Cruise, R., and L. Gardner. 2006. "Measurement and prediction of geometric imperfections in structural stainless steel members." *Struct. Eng. Mech.* 24 (1): 63–89. https://doi.org/10.12989/sem.2006.24.1.063.

Elkady, A., and D. G. Lignos. 2015. "Analytical investigation of the cyclic behavior and plastic hinge formation in deep wide-flange steel beam-columns." *Bull. Earthquake Eng.* 13 (4): 1097–1118. https://doi.org/10.1007/s10518-014-9640-y.

Elkady, A., and D. G. Lignos. 2018. "Improved seismic design and non-linear modeling recommendations for wide-flange steel columns."

- J. Struct. Eng. 144 (9): 04018162. https://doi.org/10.1061/(ASCE)ST .1943-541X.0002166.
- Engelmann, B. E., R. G. Whirley, and G. L. Goudreau. 1989. "A simple shell element formulation for large-scale elastoplastic analysis." In *Analytical and computational models of shells*, edited by A. K. Noor, T. Belytschko, and J. C. Simo. New York: ASME.
- FARO (Frasier and Raab Orthopedics). 2016. FARO edge and FARO laser ScanArm edge manual. Lake Mary, FL: FARO.
- FEMA (Federal Emergency Management Agency). 2009. *Quantification of building seismic performance factors*. Rep. No. FEMA-P695. Washington, DC: FEMA.
- Fogarty, J., and S. El-Tawil. 2015. "Collapse resistance of steel columns under combined axial and lateral loading." J. Struct. Eng. 142 (1): 04015091. https://doi.org/10.1061/(ASCE)ST.1943-541X.0001350.
- Fogarty, J., T.-Y. Wu, and S. El-Tawil. 2017. "Collapse response and design of deep steel columns subjected to lateral displacement." J. Struct. Eng. 143 (9): 04017130. https://doi.org/10.1061/(ASCE)ST.1943-541X .0001848.
- Huang, Y., and S. A. Mahin. 2010. Simulating the inelastic seismic behavior of steel braced frames including the effects of low-cycle fatigue. Rep. No. PEER 2010/104. Berkeley, CA: Pacific Earthquake Engineering Research Center, Univ. of California at Berkeley.
- Lee, Y. S., M. M. Kirka, J. Ferguson, and V. C. Paquit. 2020. "Correlations of cracking with scan strategy and build geometry in electron beam powder bed additive manufacturing." *Addit. Manuf.* 32 (Mar): 101031. https://doi.org/10.1016/j.addma.2019.101031.
- Lin, Y. K. 1996. Probabilistic theory of structural dynamics. Melbourne, FL: Robert E. Krieger Publishing.
- McAnallen, L. E., D. A. Padilla-llano, X. Zhao, C. D. Moen, B. Schafer, and M. R. Eatherton. 2014. "Initial geometric imperfection measurement and characterization of cold-formed steel C-section structural members with 3D non-contact measurement techniques." In *Proc., Annual Stability Conf. Structural Stability Research Council Toronto, Canada*. Chicago, IL: Structural Stability Research Council.
- NIST. 2010. Evaluation of the FEMA P695 methodology for quantification of building seismic performance factors. NIST GCR 10-917-8. Gaithersburg, MD: NIST.
- Schafer, B. W., and T. Peko. 1998. "Computational modeling of coldformed steel: Characterizing geometric imperfections and residual

- stresses." *J. Constr. Steel Res.* 47 (3): 193–210. https://doi.org/10.1016/S0143-974X(98)00007-8.
- Sediek, O. A., T.-Y. Wu, S. El-Tawil, and J. McCormick. 2020a. "Experimental evaluation and numerical modeling of wide-flange steel columns subjected to constant and variable axial load coupled with lateral drift demands." J. Struct. Eng. 146 (3): 04019222. https://doi.org/10.1061/(ASCE)ST.1943-541X.0002499.
- Sediek, O. A., T.-Y. Wu, J. McCormick, and S. El-Tawil. 2020b. "Collapse behavior of hollow structural section columns under combined axial and lateral loading." *J. Struct. Eng.* 146 (6): 04020094. https://doi.org/10 .1061/(ASCE)ST.1943-541X.0002637.
- Selvaraj, S., and M. Madhavan. 2018. "Geometric imperfection measurements and validations on cold-formed steel channels using 3D noncontact laser scanner." *J. Struct. Eng.* 144 (3): 04018010. https://doi.org/10.1061/(ASCE)ST.1943-541X.0001993.
- Soong, T. T., and M. Grigoriu. 1993. *Random vibration of mechanical and structural systems*. Englewood Cliffs, NJ: Prentice Hall.
- Vamvatsikos, D., and C. A. Cornell. 2002. "Incremental dynamic analysis." *Earthquake Eng. Struct. Dyn.* 31 (3): 491–514. https://doi.org/10.1002/eqe.141.
- Wu, T.-Y., S. El-Tawil, and J. McCormick. 2018a. "Highly ductile limits for deep steel columns." *J. Struct. Eng.* 144 (4): 04018016. https://doi.org /10.1061/(ASCE)ST.1943-541X.0002002.
- Wu, T.-Y., S. El-Tawil, and J. McCormick. 2018b. "Seismic collapse response of steel moment frames with deep columns." J. Struct. Eng. 144 (9): 04018145. https://doi.org/10.1061/(ASCE)ST.1943 -541X.0002150.
- Wu, T.-Y., S. El-Tawil, and J. McCormick. 2019. "Effect of cyclic flange local buckling on the capacity of steel members." *Eng. Struct*. 200 (Dec): 109705. https://doi.org/10.1016/j.engstruct.2019.109705.
- Zeinoddini, V. M., and B. W. Schafer. 2012. "Simulation of geometric imperfections in cold-formed steel members using spectral representation approach." *Thin Walled Struct*. 60 (Nov): 105–117. https://doi.org/10.1016/j.tws.2012.07.001.
- Zhao, X., M. Tootkaboni, and B. W. Schafer. 2015. "Development of a laser-based geometric imperfection measurement platform with application to cold-formed steel construction." *Exp. Mech.* 55 (9): 1779–1790. https://doi.org/10.1007/s11340-015-0072-7.